EIT Spectroscopy in Hollow Core Fibers

Masterthesis

Josephine Gutekunst

15. December 2016

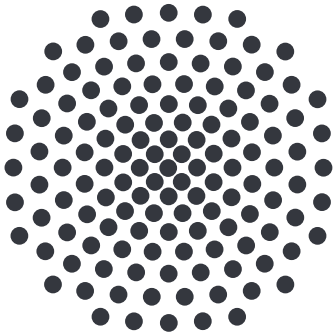

Universität Stuttgart

5. Physikalisches Institut

Examiner: Prof. Dr. Tilman Pfau

Second Examiner: Prof. Dr. Martin Dressel

Ehrenwörtliche Erklärung

Ich versichere hiermit ehrenwörtlich mit meiner Unterschrift, dass

- ich die Arbeit selbständig verfasst habe,
- ich keine anderen als die angegebenen Quellen benutzt habe und alle wörtlich oder sinngemäß aus anderen Werken übernommenen Aussagen als solche gekennzeichnet habe,
- die eingereichte Arbeit weder vollständig noch in wesentlichen Teilen Gegenstand eines anderen Prüfungsverfahrens gewesen ist,
- ich die Arbeit weder vollständig noch in Teilen bereits veröffentlicht habe,
- der Inhalt des elektronischen Exemplars mit dem des Druckexemplars übereinstimmt.

Declaration of Authorship

I herby garanty with my signiture, that

- I wrote this thesis on my own,
- I did not use any other sources than those reffered to and that I marked all literal and analogous statements,
- this thesis is neither whole nor partly part of a different examination
- the content of the electronic and the printed exemplar coincide.

Josephine Gutekunst

Stuttgart, 15.12.2016

Summary

In this thesis absorption spectroscopy of a thermal atomic vapor inside hollow core optical fibers is studied. Two different types of hollow core fiber samples are examined for diffusion behavior and sub-doppler and EIT spectroscopy. The first sample consists of a capillary of an inner-diameter of 56 μm, with conventional optical fibers spliced on each end. It was shown that this fiber can be filled with rubidium gas and that the transmission efficiency is suitable for absorption spectroscopy measurements. Sub-doppler spectroscopy was also examined. The second sample consists of a conventional vapor cell with two different fiber types mounted inside, a capillary and a kagomé style photonic crystal fiber. Two of these samples were prepared, one with fibers of inner-diameter of 60 μm and the other one with fibers of an inner-diameter of 20 μm. The diffusion in and out of these fibers were analyzed to study the effects of LIAD measurements and a theoretical model to explain the behavior was constructed. The results were compared to previous results for fibers in a conventional vacuum chamber. Additionally EIT measurements haven been performed for both core sizes, to evaluated possible applications such as quantum nonlinear optics or the study of optical bistabilities inside the hollow core of an optical fiber.

Zusammenfassung

In dieser Arbeit wurden Absorptionspektroskopie von thermischem Dampf in einer Hohlkernfaser durchgeführt. Dazu wurden zwei unterschiedliche Arten von Proben mit Hohlkernfasern in Bezug auf Diffusion, Sub-Doppler-Spektroskopie und EIT untersucht. Die erste Probe bestand aus einer Kapillare mit einem Innendurchmesser von 56 μm, die an jedem Ende mit einer Glasfaser verbunden war. Es wurde gezeigt, dass diese Hohlkernfaser mit Rubidium gefüllt werden konnte und dass die Transmissionseffizienz geeignet war um Spektroskopiemessungen durchzuführen. Außerdem wurden mit ihr Sub-Doppler-Spektroskopiemessungen durchgeführt. Die zweite Probe bestand aus einer herkömmlichen Dampfzelle, in der zwei unterschiedliche Hohlkernfasern befestigt waren, das eine war eine Kapillare und das andere eine Kagomé Kristallfaser. Von dieser Probenart wurden zwei Stück gefertigt, in der einen befanden sich Hohlkernfasern mit einem Innendurchmesser von 60 μm und in der anderen mit 20 μm. Die Fasern mit den unterschiedlichen Durchmessern wurden durch LIAD Messungen auf ihr Diffusionsverhalten untersucht und ein theoretisches Modell aufgestellt um diese zu erklären. Die Ergebnisse wurden mit früheren Ergebnissen von Fasern in einer herkömmlichen Vakuumapparatur, verglichen. Schließlich wurden noch EIT Messungen in allen Fasern durchgeführt um mögliche Anwendungen zu untersuchen, wie

zum Beispiel nichtlineare Quantenoptik oder die Untersuchung optischer Bistabilitäten innerhalb der Hohlkernfasern.

Contents

1 Introduction

The aim of this thesis is to gain further insight into the combination of Rydberg spectroscopy in atomic vapor and hollow core optical fiber. By combining the two very active fields of research and technology, an encouraging route towards future applications is pursued.

Highly excited atoms, so called Rydberg atoms, have a very high polarizability. This makes them exceptionally sensitive to outer disturbances, such as electromagnetic fields. Consequently, they are a promising building block for high performance sensing applications, such as magnetometry or electric field sensing. Additionally, they show a strong long-range interaction among themselves, which induces shifts of the energy levels. This enables the effect of the Rydberg blockade [1], which opens a whole new path for things such as an optical quantum gate, and also the possibility of optical nonlinearities at the single photon level.

Implementing Rydberg atoms into hollow core fibers is a promising concept to obtain miniaturized, integrable, room-temperature devices. It is aimed to combine the best of two worlds: On the one hand, hollow core photonic crystal fibers show low loss light guidance, and provide the possibility to be filled with fluids or gases. Compared to spectroscopy in conventional vapor cells, another major advantage is the large overlap between the light field and the atomic ensemble.

On the other hand, Rydberg spectroscopy of thermal atomic vapor provides a traceless means to realize an electromagnetic field sensor, with high sensitivity. Measurements in alkali filled hollow core fibers have been done in various experiments using vacuum chambers (e.g. [2–4]), proving the general feasibility. For real-life applications however, the somewhat bulky steel-chamber has to be eliminated, and portable samples are necessary.

In this thesis, two different hollow core fiber samples are examined. Both of them do not require a vacuum chamber setup, except for the initial filling process of the fibers. The first sample is a capillary with optical fibers spliced to each end. As it turns out, the transmission efficiency of the sample allows for absorption spectroscopy, and the rubidium vapor density within the capillary can be controlled. It was further investigated if spectroscopy of sub-doppler features is feasible. The second sample contains two different types of hollow core fibers mounted inside a conventional glass vapor cell. One fiber is a capillary, the other a kagome-style hollow core photonic crystal fiber. The fibers in each sample have the same core diameter, and samples with 60 μm and 20 μm have been prepared. The fibers are examined for their diffusion properties via temperature changes, and the effect of light induced atomic desorption for each diameter was studied. Finally, EIT measurements were conducuted, both aiming for the minimal achievable linewidth and the

possibility to enable optical bistability.

The thesis can be seen as a description of two separate projects discerned by the different sample types, and is structured as follows. First, the theoretical background necessary to understand the following measurements is layed out in section 2. In Section 3, the sample with attached optical fibers gets examined. The vapor cell with integrated fiber samples is discussed in section 4. For both projects, first the optical setup and a precise description for the preparation of the fiber-samples is given, before the results are discussed. The thesis concludes with an outlook in section 5.

2 Basics

2.1 Rubidium

In this thesis, the spectroscopy measurements are done in a thermal vapor cell containing a rubidium gas. Rubidium belongs to the group of the alkali metals and has therefore only one valence electron. It has two isotopes, one stable (^{85}Rb with a relative natural abundance of 72 %) and one quasi-stable (the ^{87}Rb with a relative natural abundance of 28 % and a life time of $4.9 \cdot 10^{10}$yr). Since the ^{85}Rb is stable and yields higher atomic densities (at the same pressure) than the ^{87}Rb, all measurement which did not cover the "whole" rubidium spectra (see figure (2)) were done with the ^{85}Rb isotope. In table (1) some physical values are listed.

		^{85}Rb	^{87}Rb
Atomic number	Z	37	37
Total Nucleons	$Z + N$	85	87
Nuclear Spin	I	5/2	3/2
Atomic mass	m	84.91 u	86.91 u
Density	$\rho_m(25° \text{ C})$	1.53 g/cm^3	1.53 g/cm^3
Vapor Pressure	$P_v(25° \text{ C})$	$5.23 \cdot 10^{-7}$ mbar	$5.23 \cdot 10^{-7}$ mbar

Table 1: Some selected numbers for the two rubidium isotopes, taken from [5].

In figure (1) the energy levels of rubidium are visualized for the D1- and D2-Line separately. The resulting absorption spectra for the two transitions can be seen in figure (2).

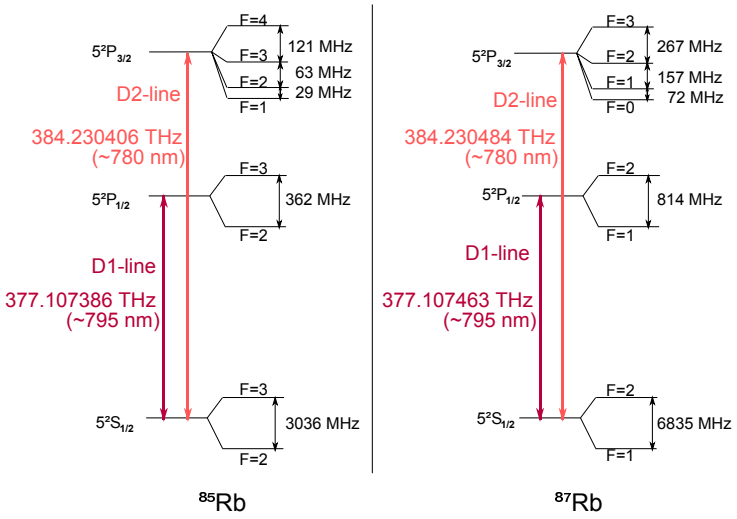

Figure 1: Energy levels of the rubidium D1-Line (795 nm) and D2-Line (780 nm) for both rubidium isotopes.

The frequency axis shows the relative frequency difference between the absorption dips and not the absolute frequency for matters of lucidity. The lamb-dips result from the fact that these are saturation absorption spectroscopy measurements (see section 2.2.3 for more details).

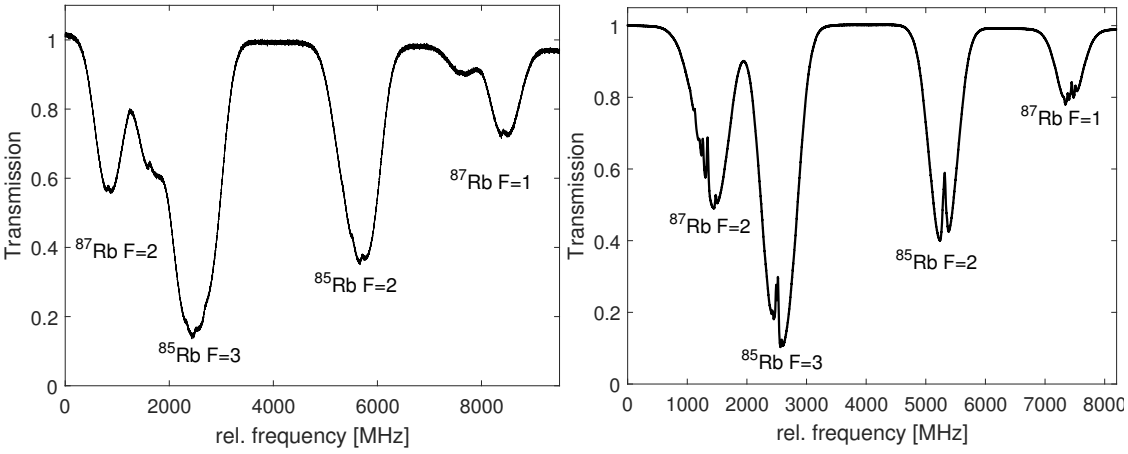

(a) D1 line

(b) D2 line

Figure 2: Absorption spectra in rubidium. Both absorption lines are scanned over both isotopes and done with saturation spectroscopy.

2.2 Spectroscopy of Thermal Gas

2.2.1 Optical Density

When light travels through a medium a portion of it gets absorbed. Typically, the underlying mechanism is the excitation of atoms into higher electronic states. The electrons then fall back into their ground state through spontaneous emission, sending light in all spatial directions. The intensity I in direction of propagation thus drops. In the case of an intensity independent absorption coefficient α it follows the Beer–Lambert law

$$I(z) = I_0 \exp[-\alpha z], \tag{1}$$

where z is the distance the light traveled in propagation direction and I_0 the incident intensity. A good measure of the absorbed light over the distance Δz is given by the optical density

$$\mathrm{OD} = \alpha \Delta z. \tag{2}$$

Since α is proportional to the population density the OD is proportional to the density of the medium and can therefore be used as an indicator for it.

2.2.2 Broadening Mechanisms

In spectroscopy measurements the observed spectral lines are not strict monochromatic. There are different broadening mechanisms that lead to distinct half widths. The most important ones in the case of a thermal gas will be discussed in the following section.

The *natural linewidth* originates from the fact that the atomic states have a natural lifetime τ. The transition of an atom can be viewed as a damped harmonic oscillator, where the damping comes from the natural lifetime of the involved states. This results in a Lorentz-profile for the observed spectral line [6]

$$L(\omega) = \frac{A_{k,i}/2\pi}{(\omega - \omega_0)^2 + (A_{k,i}/2)^2} \quad . \tag{3}$$

with the normalization

$$\int_0^\infty L(\omega)\mathrm{d}\omega = 1 \tag{4}$$

Here ω_0 is the eigenfrequency of the system and $A_{k,i}$ the Einstein coefficient of the transition from state k to i. This results in a line width of $\omega_L = 1/\tau_k + 1/\tau_i$.

For the spectroscopy of thermal gas the movement of the atoms also plays an important role. Because of the movement the observed frequency shifts from the eigenfrequency ω_0 to $\omega = \omega_0 - \mathbf{k} \cdot \mathbf{v}$, dependent of the velocity $\mathbf{v}$ of the atoms and the wave vector $\mathbf{k}$ of the emitted light. The Maxwell-Boltzmann distribution leads to an overlap of the different shifts, resulting in a Gaussian profile [6]

$$G(\omega) = \exp\left[-4\ln(2)\left(\frac{\omega - \omega_0}{\omega_D}\right)^2\right]. \tag{5}$$

This is called *Doppler broadening* with the Doppler width of $\omega_D = \frac{\omega_0}{c}\sqrt{\frac{2k_BT \cdot 4\ln(2)}{m}}$.

The *pressure broadening* is also an important broadening mechanism. It emerges when two atoms collide or get close to each other. The interaction leads to a shift of the energy levels and a reduction of the life time of the excited state. For an elastic collision the energies only get shifted during the collision and the line shiftes by $\Delta\omega = \omega_0 - \frac{|E_A(R) - E_B(R)|}{\hbar}$, where the energies of the atoms A and B are dependent on the distance R between the atoms. For an inelastic collision the energy of the collision partners gets (for a part or as whole) translated into inner energy or kinetic energy. As a result of both processes, the line is broadened resembling a Lorentzian profile.

Another broadening mechanism is caused by the laser power and called *power broadening*. The population density of the ground state of a two level atom depends on the pumprate P of the laser and the relaxation probability R_1, R_2 of the involved states. For high values of P the population difference is given by

$$\Delta N = \frac{\Delta N(P = 0)}{1 + S} \qquad \text{with} \quad S = \frac{2P}{R_1 + R_2}. \tag{6}$$

For $R_1 = 0$ the saturation parameter S can be written as $S(\omega) = \frac{2\sigma_{12}(\omega)I(\omega)}{\hbar\omega A_{12}}$, being dependent on the intensity I of the laser. Since the absorption coefficient $\alpha = \frac{\alpha_0}{1+S}$ gets a frequency dependency through the saturation parameter the line gets broadened with

$$\Delta\omega_S = \Delta\omega_0 \sqrt{1 + S(\omega = \omega_0)}. \tag{7}$$

2.2.3 Saturation Spectroscopy

In spectroscopy measurements the Doppler effect often leads to the fact that close spectral lines can not be resolved because of an overlap of the Gauss-curves. To improve the resolution a *saturation spectroscopy* can be conducted. In figure (3) the setup of such a system can be seen. The initial beam is split into two arms and overlapped inside of the cell counter-propagating. The pump beam has a much higher laser intensity than the probe beam, which is detected with a photodiode.

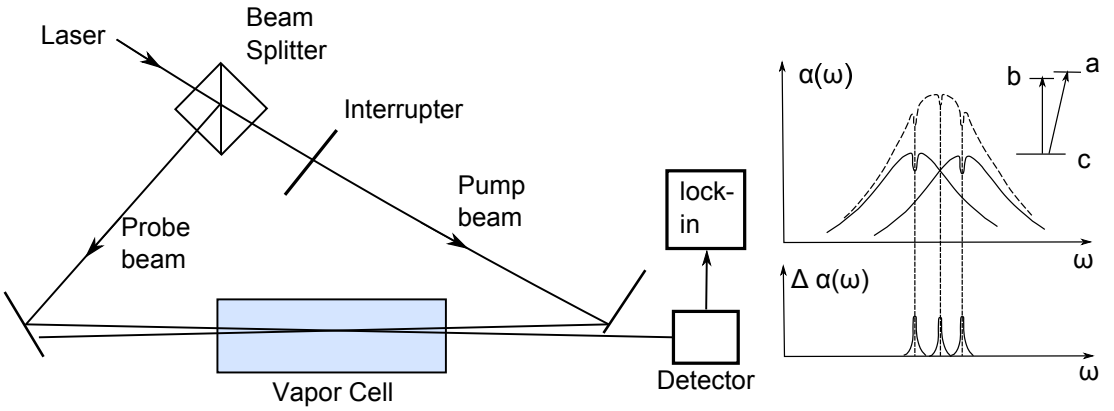

Figure 3: Saturation spectroscopy (after [7]). Setup (left): The beams are coupled into the vapor cell counter-propagating, the probe beam gets detected and the signal amplified with a lock-in-amplifier. Absorption signal of the probe beam (right). Top: signal for two near atom levels, bottom: lock-in-amplified difference signal.

If the laser is off-resonant the two beams can still excite atoms which compensate the frequency shift through the Doppler effect. This holds true for different atoms for the two lasers since they are counter-propagating. Therefore both beams weaken in intensity while traveling through the vapor cell.

If however the laser is resonant, the two beams can only excite atoms with zero velocity component parallel to the beam direction. This means both beams address the same atoms. Since the pump laser has a much higher intensity, it pumps away most atoms from the ground state and the probe beam does not get absorbed as much. As a result peaks can be seen in the spectra for

on-resonant frequencies (see figure (3) right top). These are called lamb-dips. Right in the middle of the resonance frequencies of two hyperfine states an additional lamb-dip appears, the so called cross-over-resonance. It appears because at this frequency the two lasers excite the same moving atom into the different exited states due to the Doppler shift.

The signal-to-noise ratio of the signal can be improved with the help of a lock-in amplifier. To do this the pump laser is modulated with an interrupter so that the appearance of lamb-dips in the probe signal gets modulated accordingly. The lock-in amplifier now amplifies the signal through phase-sensitive detection. Additionally the Gaussian background of the spectrum can be removed (see figure (3) right bottom) with a differential lock-in-amplifier, which amplifies the difference of the signal with and without the pump beam.

2.3 Hollow Core Fibers

Hollow core fibers have, as the name indicates, a hollow core in contrast to solid core fiber or conventional optical fibers. This core can be filled with gas or liquid which then overlaps very well with light guided alongside the fiber core. In optical fibers the guiding mechanism is based on total internal reflection of the light at the cladding with a lower refractive index than the core. For hollow core fibers this is not possible since there is no cladding material with $n < 1$ available. Here the guiding mechanisms are based on different effects, depending of the structure of the fiber. In general there are three different fiber types: the capillaries, the bandgap hollow-core photonic fibers (BG-HCPCF) and the kagomé lattice fibers.

The core of the BG-HCPCF is surrounded by a honey-comb lattice which builds up a band-gap. This band-gap results in frequency domains in which light can not travel through the fiber and gets trapped in it. The BG-HCPCF usually have a very narrow transmission band width of around 100 nm.

In this thesis the fibers used are the capillary and the kagomé fiber. Therefore these two will be discussed in more detail.

2.3.1 Capillary

Capillaries guide the light via nearly total reflection for gracing incidence.There are three light modes in general allowed inside the capillary: the transverse electric modes (TE), the transverse magnetic modes (EH) and hybrid modes (EH). For low orders these modes can be seen in figure (4). For in-coupled Gaussian beams

$$E(r) = E_0 \exp(-r^2/\omega^2) \tag{8}$$

only EH_{1m} field modes can be excited [8]. They can be approximated with the Bessel-function J

$$E(r) = E_0 J_0(u_m \frac{r}{a}) \tag{9}$$

for fibers of radius a. u_m is the m-th root of the zero order Bessel function J_0. For the lowest loss mode EH_{11}, the highest coupling efficiency of 98.1% is reached for a beam waist to core ratio of $\omega/a = 0.64$ [8].

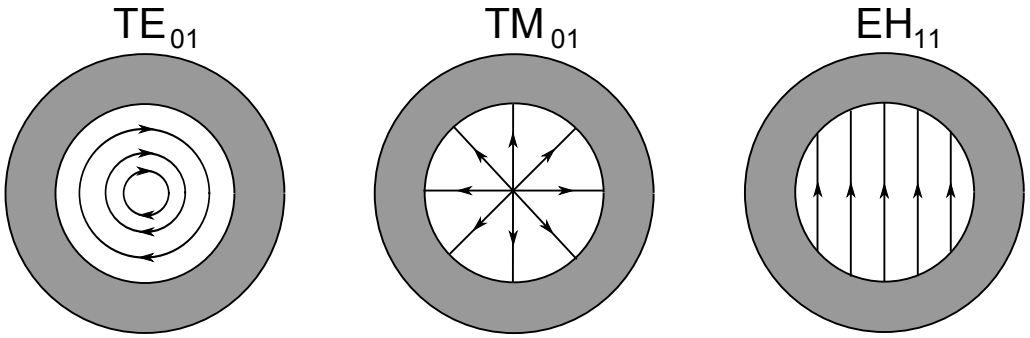

Figure 4: Schematics for possible light fields inside a hollow core fiber. Given are low order modes of transverse electric (TE), transverse magnetic (TM) and hybrid (EH) field modes. For Gaussian beams the EH_{11} is the lowest loss mode.

2.3.2 Kagomé

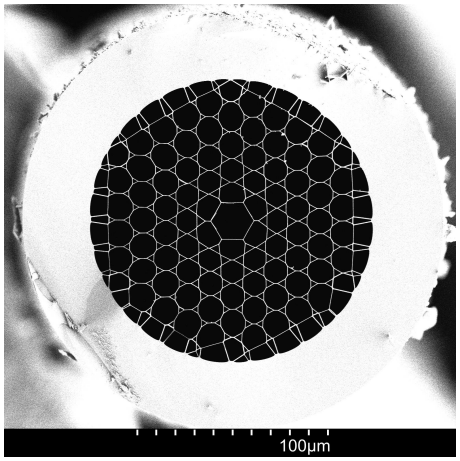

Figure 5: SEM picture of the cross section of a kagomé fiber (picture provided by the MPL Erlangen Russell division). The core in the middle is surrounded by the kagomé lattice structure and encased in the glass cladding.

The kagomé fiber gets its name from its trihexagonal lattice structure surrounding the core (figure (5)). Even though at first thought this seems comparable to the bandgap fibers, which are

surrounded by a honeycomb lattice structure, the guiding mechanism of the kagomé is based on a different effect. The kagomé fiber has no bandgap that confines the light, rather anti-resonance properties in the first ring of holes provide the guidiance of the light [9]. In comparison to bandgap fibers this leads to broader transmission bands but also to higher losses.

2.4 Diffusion in Thin Tubes

The propagation of light in hollow core fibers has been discussed in the previous section. In this section the propagation of atoms inside the core is discussed.

The diffusion properties of gas into a thin tube are determined by the Knudsen number $K_n = \frac{\lambda}{2r}$, with λ being the mean free path of the gas molecules and r the radius of the tube. If $K_n \ll 1$ it means that the gas molecules mainly collide with each other and that collision with the tube wall can be neglected and the dynamics can be described by the Navier-Stokes-equations. If $K_n \gg 1$ (which will be the case in this thesis) the molecules have a long mean free path and collide mainly with the tube wall. The dynamics in this case can be described with a one-dimensional diffusion equation [10]

$$\frac{\partial n}{\partial t} = D\frac{\partial^2 n}{\partial x^2}. \tag{10}$$

Here $n(x,t)$ is the atomic density inside the thin tube for the time t at position x and D is the diffusion constant, which for thin tubes is given by [10]

$$D = \frac{4}{3}\frac{r^2}{\tau + (2r/\bar{v})}. \tag{11}$$

Here $\bar{v} = \sqrt{8k_BT/(\pi m)}$ is the mean velocity of the gas atoms with their mass m. The adsorption time τ is dependent on the adsorption energy E_a, the temperature of the tube wall T_w and the characteristic absorption time τ_0:

$$\tau = \tau_0 \exp\left[\frac{E_a}{k_BT_W}\right]. \tag{12}$$

τ can be interpreted as the mean time an adsorbed atom stays on the wall and is therefore inverse proportional to the adsorbtion rate $\nu = 1/\tau$. The solution of the diffusion equation (10) can be seen in figure (6) for a thin tube of lenght l and with the following boundary conditions:

$$\begin{aligned} &n(t=0,x) = 0 && \text{for } -l/2 < x < l/2 \\ &n(t, x = \pm l/2) = n_0 && \text{for all } t. \end{aligned} \tag{13}$$

The tube is empty at time $t = 0$ and gets filled via diffusion from the surrounding atomic density n_0. In [3] the filling time of a thin tube is defined as the time when the density inside the tube

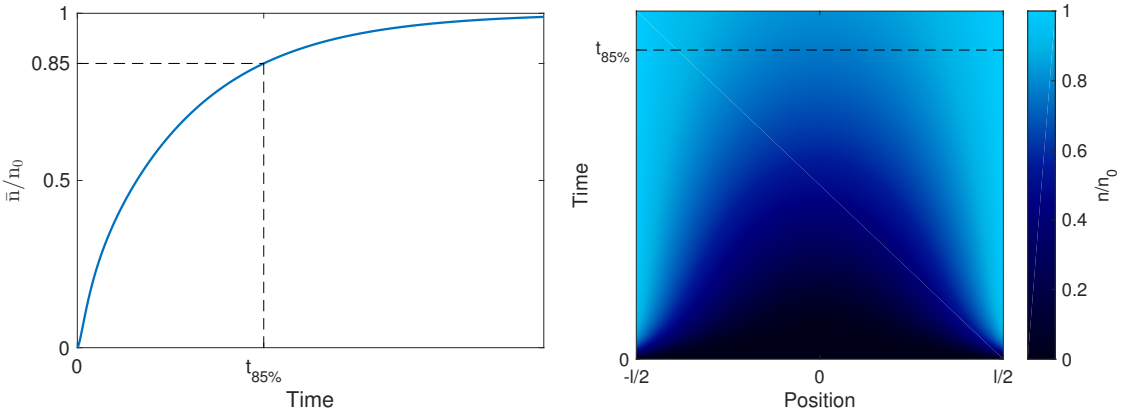

(a) Spatally averaged density inside tube

(b) Density evolution in tube

Figure 6: Solution of the diffusion equation (10) for a tube of length l and the boundary conditions (13). (a) is the filling curve of the tube over time, where $\bar{n}$ is the density averaged over all positions in the fiber. (b) shows the evolution of the density over time and position.The filling time $t_{85\%}$ is marked in both pictures.

reaches 85% of the surrounding density and can be approximated to

$$t_{85\%} \approx 0.216\frac{l^2}{D} = 0.162\left(\frac{2l^2}{r\bar{v}} + \frac{l^2\tau}{r^2}\right). \tag{14}$$

It is strongly dependent on the length l and radius r of the tube and through $\bar{v}$ and τ also from the temperature of the system.

2.5 Surface Interactions

2.5.1 Light Induced Atom Desorption

When a glass vapor cell is exposed to an alkali gas atoms get adsorbed onto the glass surface and desorbed from it. These processes usually reach a equilibrium, only dependent on temperature (see eq.(12)) and lead to a specific vapor pressure. If light is shone onto that surface, a new desorption process takes place, leading to a rise in vapor pressure. This effect can be observed very well in hollow core fibers since here the surface to volume ratio is very large. In general, one can differentiate between two light induced desorption processes: the light induced atomic desorption (LIAD) and the surface-plasmon induced desorption (SPID). In the literature, the term LIAD is often used for both processes, as a general term for atoms desorbing from surfaces via light.

For high photon energies the LIAD process occurs. It is fast and non-thermal and grows exponentially with the photon energy. It can be attributed to the photons directly providing the energy necessary for the atoms to overcome the binding energy.

For lower photon energies the dominating effect is the SPID. For rubidium this photon energy is typically around 1.5 eV [11] which correspondes to a wavelength of around 827 nm. In this case the desorption process is caused by a surface-plasmon getting excited (heating), which then acts as a catalyst for non-thermal desorption of an atom. This leads to an effective evaporation of nanoclusters (i.e. "small droplets" of the alkalis).

A third effect should also be mentioned: the effect of light induced diffusion inside the glass bulk. Atoms do not only get adsorbed to the surface but diffuse into the bulk. If now atoms from the surface are desorbed through LIAD or SPID, atoms inside the bulk start to diffuse to the surface, where they can also get desorbed via the light. The atoms in the bulk can act therefore as a slowly depleting reservoir during the LIAD process.

2.5.2 Electric Fields Near Surfaces

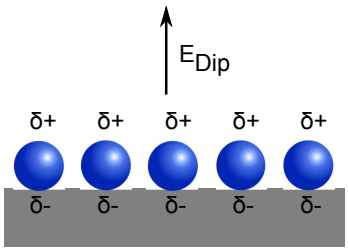

Figure 7: Induced alkali dipoles on a dielectric surface. The dipole moments create an electric field perpendicular to the surface.

When the alkali atoms adsorb to a dielectric surface they experience a charge transfer with the atoms of the surface. In the case of rubidium on a silicate surface (SiO_2) the rubidium atom binds to two oxygen atoms. Since the oxygen has the higher electro-negativity the density of the electrons is increased around the oxygen atom. This results in a dipole moment which in turn produces an e-field E_{Dip} perpendicular to the surface (see figure (7)). For rubidium on SiO_2 the dipole moment per adsorbed atom is $d_0 = 12$ D [12].

The induced e-field E_{Dip} shifts the energy level E_R of excited atoms near the surface via the stark effect

$$\Delta E_R = \frac{1}{2}\alpha_p E_{\mathrm{Dip}}^2 \tag{15}$$

depending on the polarizability α_p. The polarizability of Rydberg atoms scales with $\alpha_p \propto n^{*7}$ the effective quantum number n^*. They are therefore highly sensitive to electromagnetic fields and can be used to measure the field created by the adsorbed atoms. Rydberg atoms are often excited using

a two- or three-photon transitions. This can lead to new effects in comparison to a one-photon transition.

2.6 Electromagnetic Induced Transparency

2.6.1 Principle

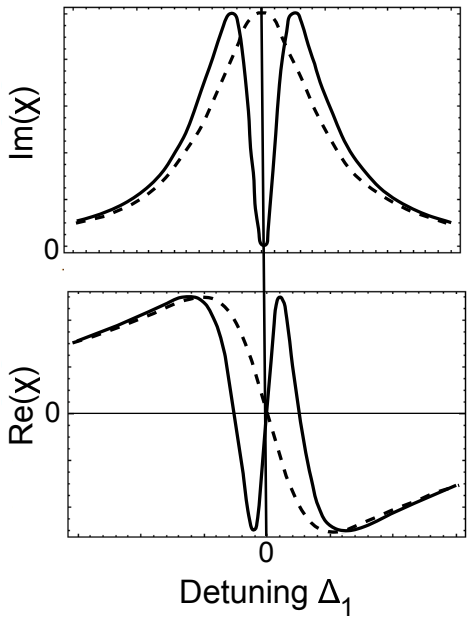

Figure 8: Real and imaginary part of the susceptibility for a two-level system (dashed lines) and an EIT system (full line) (after [13]).

In a three-level atom one can observe an effect called electromagnetic induced transparency (EIT), in which a medium gets transparent at a frequency it normally absorbs by shining in a second light field. Roughly speaking, the third level enables an additional excitation path way, which can then destructively interfere with the direct link between the two initial levels. Figure (8) the change in the susceptibility when the EIT conditions are fulfilled. The imaginary part of the susceptibility gives the frequency dependency of the absorption of a medium, while the real part gives the frequency dependency of the refractive index. They are shown in relation to the frequency shift of the probe laser.

EIT requires a three level system, with one transition being dipole-forbidden. In the case of figure (9) this is the case for the $|1\rangle - |2\rangle$ transition. The Λ scheme is the most suitable of the three depicted schemes for EIT measurements. From the ground state $|1\rangle$ the electrons are excited to the excited state $|3\rangle$ with the probe laser at a transition frequency of ω_p. The Rabi-frequency with

which this transition oscillates is given with $\Omega_p = \vec{d_p} \cdot \vec{E_p}/\hbar$, where $\vec{d_p}$ is the dipole moment of the transition and $\vec{E_p}$ the amplitude of the electric field. State $|3\rangle$ is now coupled to state $|2\rangle$ with a transition frequency of ω_c and the Rabi-frequency is Ω_c.

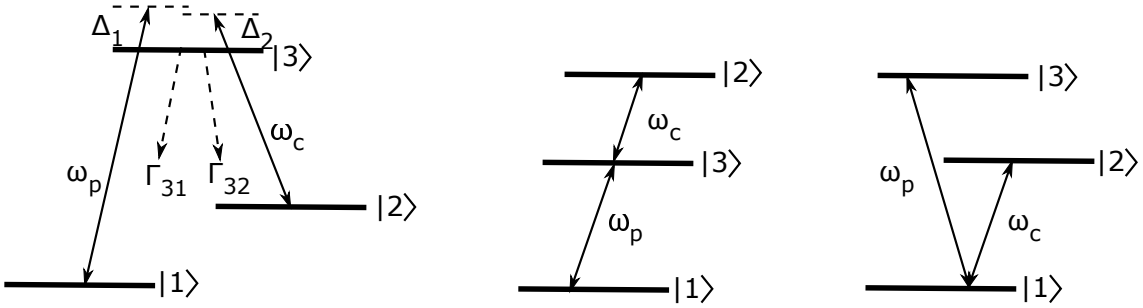

Figure 9: EIT Level schemes with the probe transition frequency ω_p and coupling transition frequency ω_c. The detuning $\Delta_{1,2}$ and the decay rates Γ are exemplary shown in the left scheme. Left: Λ-type, middle: Ladder-type, right: V-type.

The Hamiltonian describing this systems is composed of the unperturbed system of the atom hamiltonian H_0 and the interaction Hamiltonian $H_{int} = \vec{d} \cdot \vec{E}$ of the two light fields. In the rotating-wave approximation this leads to a Hamiltonian

$$H = -\frac{\hbar}{2} \begin{bmatrix} 0 & 0 & \Omega_p \\ 0 & 2(\Delta_1 - \Delta_2) & \Omega_c \\ \Omega_p & \Omega_c & 2\Delta_1 \end{bmatrix}, \tag{16}$$

with the new eigenstates:

$$\begin{aligned} |a^+\rangle &= \sin(\theta)\sin(\phi)\,|1\rangle + \cos(\phi)\,|3\rangle + \cos(\theta)\sin(\phi)\,|2\rangle \\ |a^0\rangle &= \cos(\phi)\,|1\rangle - \sin(\theta)\,|2\rangle \\ |a^-\rangle &= \sin(\theta)\cos(\phi)\,|1\rangle - \sin(\phi)\,|3\rangle + \cos(\theta)\cos(\phi)\,|2\rangle\,. \end{aligned} \tag{17}$$

Here $\tan(\theta) = \frac{\Omega_p}{\Omega_c}$ and $\tan(2\phi) = \frac{\sqrt{\Omega_p^2+\Omega_c^2}}{\Delta_1}$. Remarkably the eigenstate $|a^0\rangle$ has no contribution from state $|3\rangle$ and is therefore called dark state. If the system is in this state, it is not possible to be exited into $|3\rangle$. This dark state is only stable for the Λ-scheme, which is why it is the only scheme which shows EIT in the strict sense. The dark state can be addressed with the condition $\Omega_p << \Omega_c$ since then $\sin(\theta) = 0$ and the ground state becomes identical to the dark state.

2.6.2 Bistability

For high laser powers a bistability of the EIT signal was observed [14]. In figure (10) the evolution of the EIT signal for rising coupling beam powers P_c (respectively Rabi frequencies $\Omega_c \propto \sqrt{P_c}$)

can be seen. At first the signal only shows a shift which direction is depending on the polarizability, in figure (10) it is depicted as a red-shift. For higher laser powers however a hysteresis emerges dependent in which direction the frequency of the coupling laser is tuned. First measure-

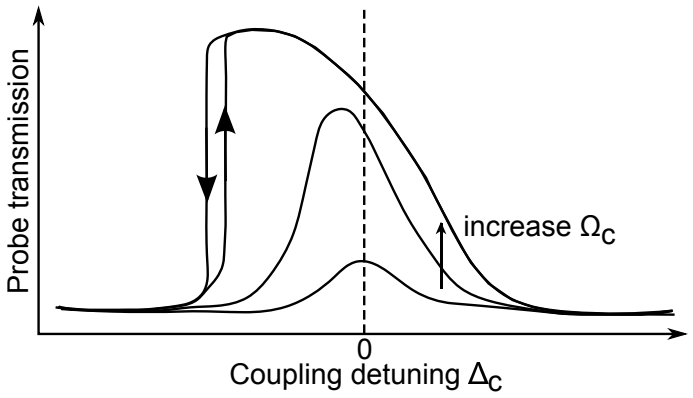

Figure 10: Bistability signal as it is observed for example in [14]. For rising coupling laser powers the signal first gets shifted and for even higher laser powers it shows a hysteresis signal. This is contributed to ions produced by collision ionization.

ments contributed this effect to dipole-dipole interactions of the Rydberg atoms [15], but present measurements [14] imply that rather interactions with ions are the cause. The hysteresis results from the competition of a non-linear energy shift due to the interaction and the decay rate from the Rydberg state. The energy shift is dependent on the Rydberg population. When the laser is scanned from the blue detuned side to the red the Rydberg population is build up and it sustains the ability to excite additional atoms even away from resonance. At a certain point the detuning however gets to large and the decay mechanism dominates. This can be seen in a sudden breakdown in the probe transmission in figure (10). When the laser is scanned from the red detuned to the blue detuned though the Rydberg population stays low in the bistable region until the detuning becomes small enough to excite the atoms.

3 Fiber Series: Spectroscopy Below the Doppler Limit

3.1 Setup

3.1.1 Cell

In this section the cell used is the fiber series, which is named for its series circuit of optical fibers and a hollow core fiber. A picture of its setup can be seen in figure (11). A single-mode Thorlabs 780HP fiber was spliced from one side onto a capillary. It was done such that the modes of the single-mode fiber (SM) and the ones of the capillary overlap, with an expected coupling efficiency of 10 % for low order modes. On the other side a multi-mode fiber (MM) was spliced onto the capillary, but only partially so that a small gap remains (see figure (11)). Through this gap the rubidium from the reservoir can diffuse into the region between the two fibers, hereafter called the interaction region. It has a length of 2 cm and the inner diameter of the capillary is 56 μm.

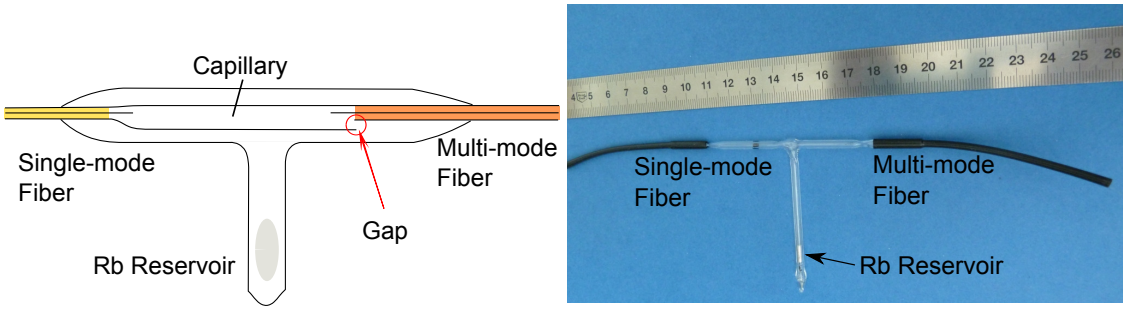

Figure 11: Structure of the glass fiber coupled cell. The single-mode and the multi-mode fiber are spliced to the capillary at the respective sides. The capillary can be filled with rubidium through the gap at the multi-mode side. The space between the fibers has a length of 2 cm and an inner diameter of 56 μm

The fiber series was filled with rubidium in the conventional way: It is attached to a pump system containing a turbo-pump and a shock seal leading to a rubidium reservoir. After the excavation to approximately 10^{-7} mbar the seal is broken and a rubidium drop is guided into the cell. To prevent damage of the brittle fiber construction the droplet was moved rather stepwise by evaporation and condensing. The cell is then ablated from the vacuum pump.

3.1.2 Oven

The oven is constructed in a way that the reservoir of the fiber series and the interaction region can be heated independently. Therefore the two parts of the oven are separated by an isolating layer of Polyetheretherketon (tecapeek) as seen in figure (12). The oven is heated with conventional cartridges inserted into the copper bottom. To control the temperature two PT100 elements are

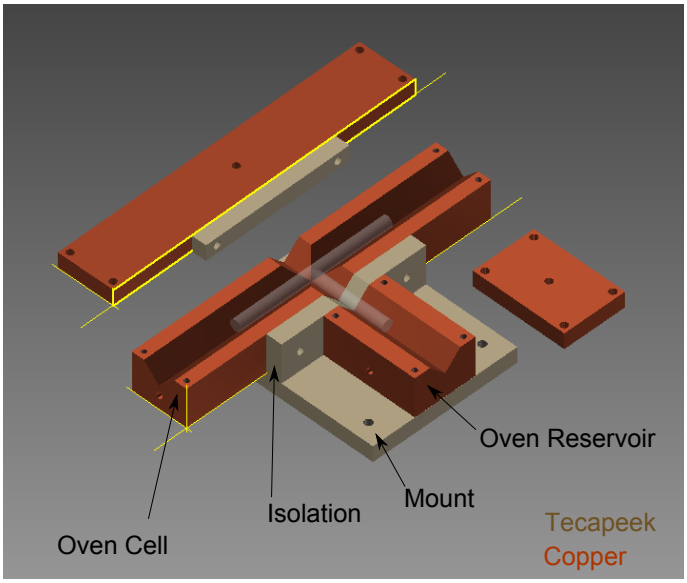

Figure 12: Schematic of the oven. The oven for the interaction region (cell) and the oven for the reservoir are separated through an isolating layer of tecapeek. The oven is heated with conventional cartridges inserted into the bottom.

used, each connected to a PID-controller, which regulate the current flowing through the heating cartridges. This setup enables it to keep the reservoir at constant 70 °C and the interaction region of the cell at 80 °C.

3.1.3 Laser Setup

The lasers and the saturation spectroscopy are set up on a different table and the laser beams are brought to the setup via optical fibers. For this experiment 780 nm and 795 nm light is used and the configuration of the beams is shown in figure (13). The 780 nm laser is coupled into the single-mode fiber and behind the multi-mode fiber the absorption signal is detected with a preamplified photodiode.

In addition the 780 nm light can also be coupled into the fiber from the multi-mode side, to allow counter-propagating beams inside the cell. This is done with a glass plate so that a small

part of the incoming light can be reflected into the fiber but the main part of the absorption signal coming out of the fiber is transmitted through the glass and detected with the photodiode.

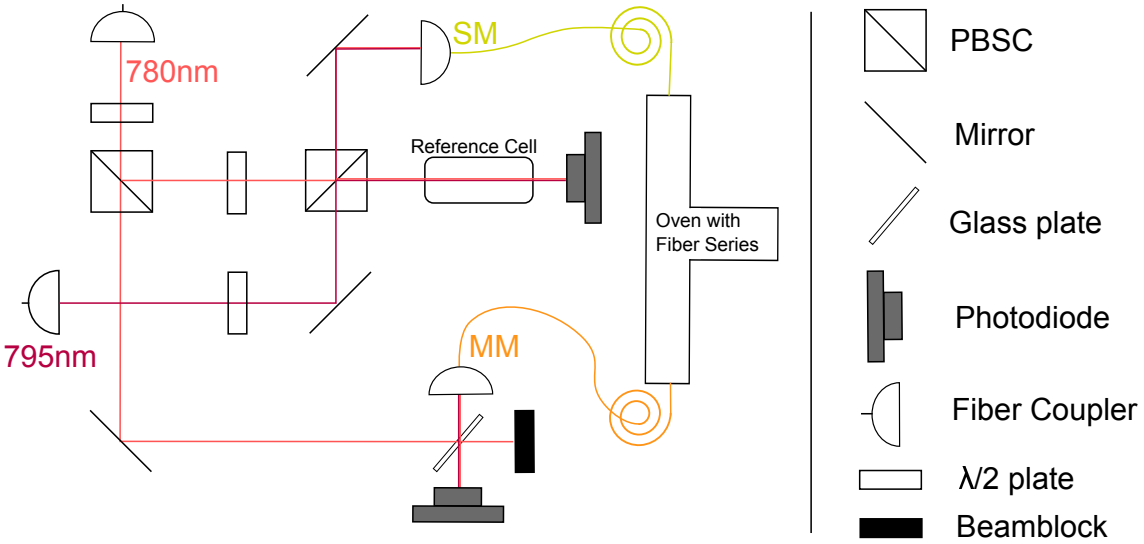

Figure 13: Schematic laser setup. The two lasers are coupled into the single-mode fiber and also lead through the reference cell co-propagating. The 780 nm light is also coupled into the multi-mode to allow counter-propagating beams inside the fiber.

Later the 795 nm laser is also coupled into the single-mode fiber to have two co-propagating beams inside the cell. With a polarizing beam splitter and two $\lambda/2$-waveplates the power of the lasers can be adjusted. The overlapped beams are also lead through a reference cell, which is a broad cell placed into the beams at room temperature. The absorption signal of this cell is recorded with another photodiode. During the experiment one of the two lasers is locked by saturation absorption spectroscopy while the other is scanned over the transition. The results of these measurements can be seen in section 3.2.4.

3.2 Results

3.2.1 Transmission

The first measurements are done before the fibers are filled with rubidium. There are two samples ready and the measurements are conducted with both. The transmission efficiency is measured by coupling 795 nm laser light into the fiber. In this case this is not done via two mirrors as introduced in figure (13) but the fiber transporting the 795 nm laser light is directly “butt-coupled” into the fiber of the cell. Since it can not be measured how well the light is coupled into the single-mode fiber the values in table (2) have to be viewed with the thought in mind, that not all of the

light reaches the interaction region. The coupling efficiency of the butt-coupler is estimated to be around 50 %. But since this could vary from fiber to fiber the values given in table (2) are the relative laser power before the butt-coupler and after the light comes out of the second fiber.

Direction	Fiber 1	Fiber 2
SM to MM	4.4%	6.6%
MM to SM	0.01%	0.03%

Table 2: Transmission efficiency of the butt-coupled fiber series

In both samples the transmission from the single-mode into the multi-mode is distinctly larger than the other way round. This is due to the fact that the multi-mode fiber collects far more light from the interaction region than the single-mode fiber and therefore the transmission in this direction is better. However the transmission in the other direction is not zero and can still be used to perform measurements.

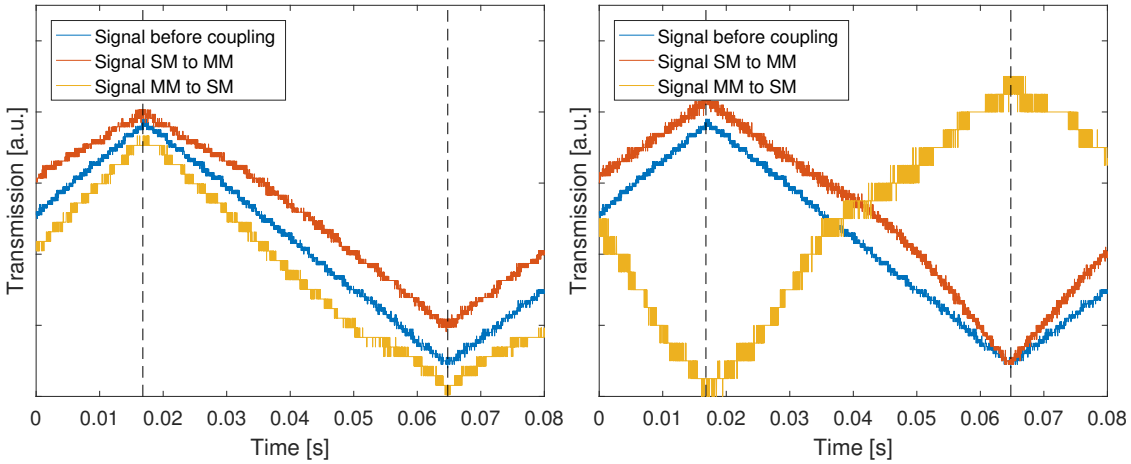

(a) Transmission in fiber 1

(b) Transmission in fiber 2

Figure 14: Transmission without rubidium in fiber for either direction. The signals are scaled to fit the same regime for the purpose of better comparison.

In the next step the laser is frequency scanned. By doing so the power of the laser changes linearly with the frequency, due to the feed-forward of the laserdiode current. The transmission of the resulting ramp is observed. For the first fiber the transmitted ramp appears as expected, even though the noise level for the multi-mode to single-mode transition is of course a little bit larger than for the other direction, as can be seen in figure (14a). To be able to compare the ramps the transmission through the fibers are scaled to fit the data into the same regime. This holds also true for the second fiber, but here we see a clear deviation for the signal when we go in the multi-mode

to single-mode direction, and with small nudges on the fiber the signal fluctuates strongly.

Fiber 1 is the first one to be filled with rubidium. Unfortunately the fibers broke, most likely during the filling or the transport of the fiber. In both, the single-mode and the multi-mode fiber, one could see a rupture under the microscope and the transmission efficiency in the direction single-mode to multi-mode dropped to 0.05%. Therefore all the following measurements are done with the second sample.

3.2.2 Absorption Spectroscopy

To measure the absorption in the D2-line, 780 nm light is coupled into the single-mode fiber and detected with a photodiode after the multi-mode fiber, as seen in figure (15a). The signal is well visible and agrees with the reference signal.

The absorption in the other direction is also measured. To do that a photodiode was placed into the setup in figure (13) in front of the single-mode fiber, measuring the out-coming light. The signal is a lot noisier because it is overlapped with an interfering signal. The better the coupling efficiency is, the stronger the interference signal gets. Most likely the laser gets reflected inside the interaction region, for example at the incoupling point into the single mode. This would explain why the interference signal is only visible in this direction. The free spectral range between two peaks is $\nu_{\mathrm{fsr}} = (31 \pm 3)$ MHz which corresponds to a cavity length of $L = (4.8 \pm 0.5)$ m, which matches the optical distance from the starting point of the single-mode fiber to the endpoint of the multi-mode fiber.

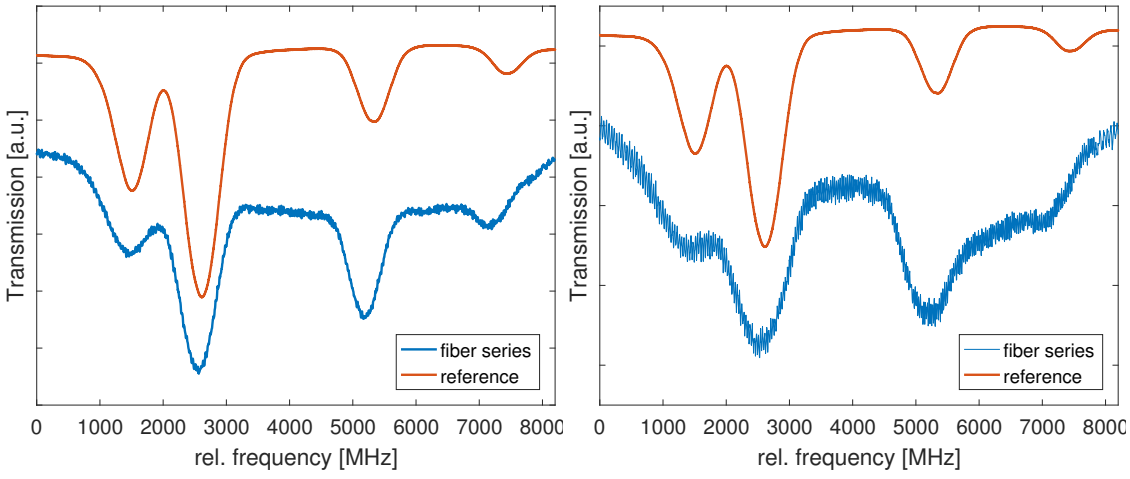

(a) Single-mode to multi-mode

(b) Multi-mode to single-mode

Figure 15: Rubidium D2-line absorption spectrum of the fiber series for light coupled in from either direction.

3.2.3 Optical Density

An interesting question is how fast the atoms can diffuse from the reservoir into the interaction region. To test this, the interaction region is left at constant 80 °C whereas the temperature of the reservoir is tuned starting from 70 °C down to 45 °C and back up again. While in the lower temperature regime the density in the reservoir should drop and therefore the rubidium-atoms from the interaction region should diffuse into the reservoir and the optical density inside the interaction region should in turn decline.

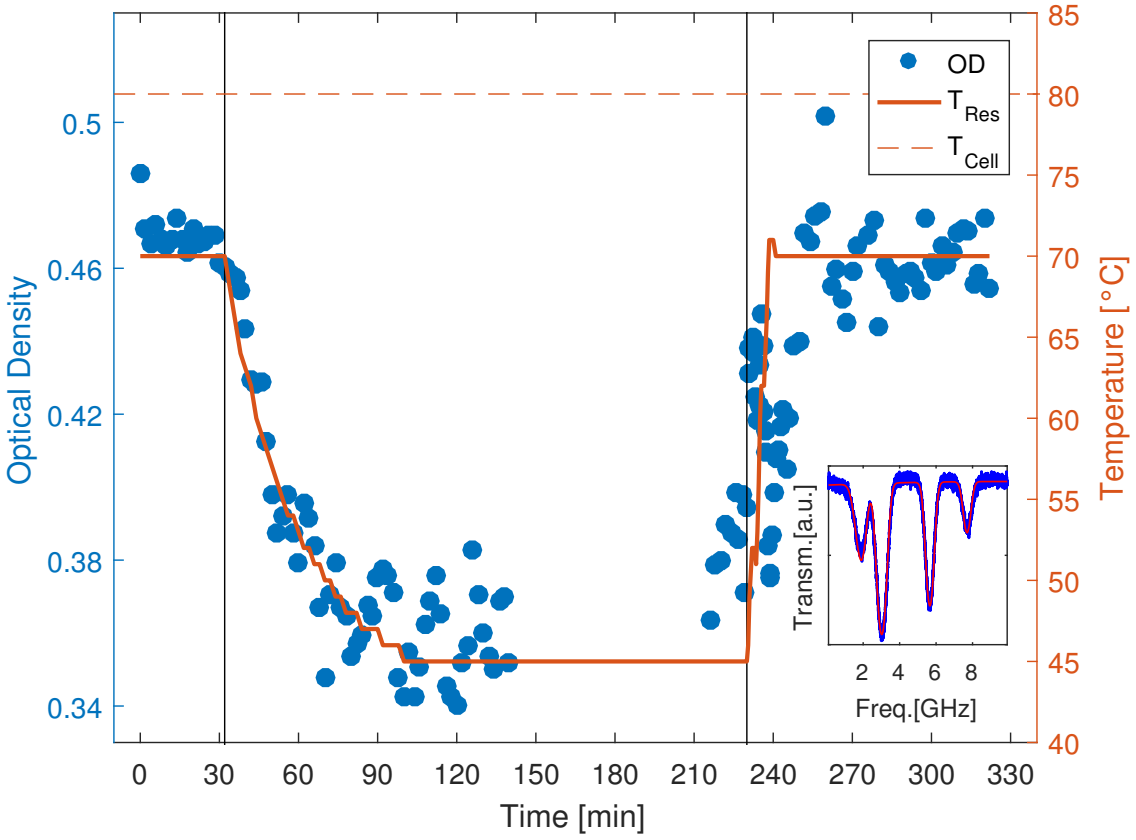

Figure 16: Variation of the optical density over time with temperature changes. The cell temperature is kept constant at 80 °C while the reservoir temperature is changed. Inset: Gaussian-fit (red) to absorption data (blue), by which the OD is determined.

To measure the density the absorption spectra of the D1-Line is recorded in the single-mode to multi-mode direction and a gauss function is fitted to it, taking into account all transitions (see inset figure(16)). From the fit-parameters the optical density is calculated. In figure (16) it can be seen, that the optical density follows the temperature without delay but shows then strong fluctuations which do not fade out within the next two hours. When the temperature rises up again, the optical

density follows again nearly instantaneous and reaches a density a bit smaller and with stronger fluctuations than before. Again, it will take several hours until the system equilibrates.

3.2.4 Subdoppler Spectroscopy

The goal of this section is to see if sub-doppler spectroscopy in the fiber series is possible and if there is a difference to a conventional broad cell. Therefore the 780 nm light is coupled into the fiber series from both sides, to do a saturation spectroscopy. The resulting spectra can be seen in figure (17). There are no lamb dips visible, but instead again a strong interference signal similar to section 3.2.2, but in this case it also shows a beat. The free spectral range of the two initial signals is $\nu_{\mathrm{fsr},1} = (28 \pm 2)$ MHz and $\nu_{\mathrm{fsr},2} = (45 \pm 5$ MHz). The smaller one agrees with the interference signal measured in the absorption signal of section 3.2.2, the second is larger but still in the same regime. Because of this interference signal measurements with counter-propagating beams seem disadvantageous. Since the problem with the interference signal only appears for the coupling process multi-mode to single-mode side, sub-doppler spectroscopy is much more feasible if both lasers are coupled into the fiber in the same direction. For this purpose two laser beams of different

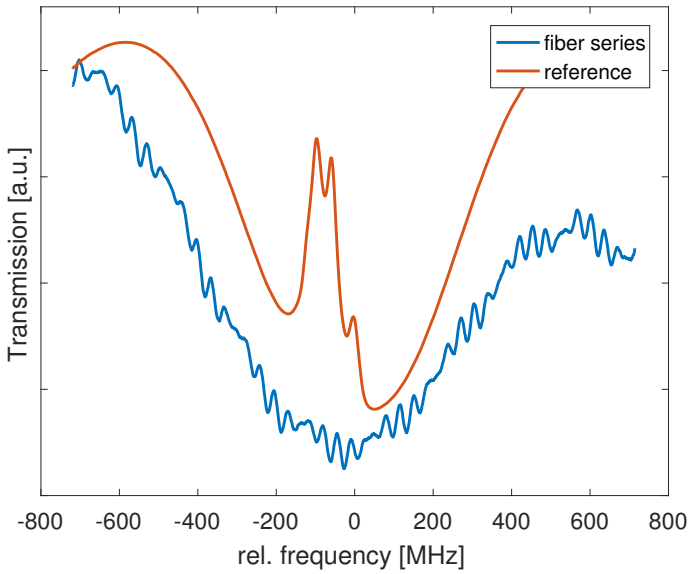

Figure 17: Saturation spectroscopy inside the fiber series with reference measurement in a conventional broad vapor cell.

wavelength, respectively the one driving the D1-transition and the other driving the D2-transition - are coupled into the fiber series and the reference cell in co-propagating configuration. In the case shown in figure (18), the 780 nm laser is locked onto the transition from the hyperfinelevel $^{85}\mathrm{Rb}\ 5S_{1/2}F = 3$ to the $5P_{3/2}F' = 4$ and used as probe beam, while the 795 nm laser scanning

over the the hyperfeinlevels of the D1-transition workes as pump beam. Since both beams reach the photodiode, a bandpass-filter is mounted onto the photodiode that only lets the 780 nm light pass and blocks the 795 nm.

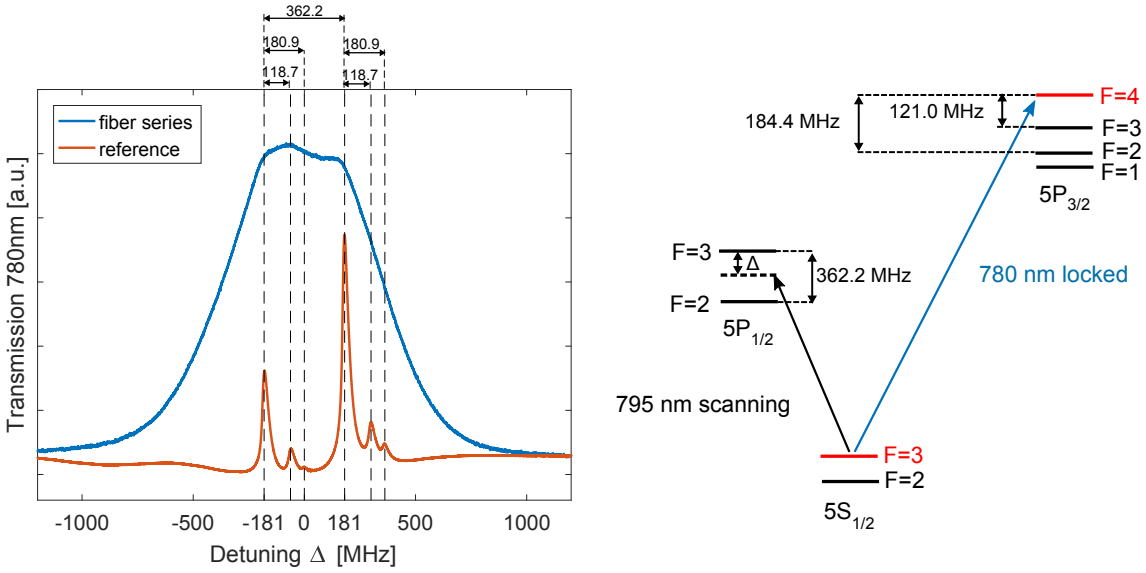

Figure 18: Sub-doppler spectroscopy with co-propagating 780 nm and 795 nm beams inside the fiber array and a conventional broad vapor cell. The laser powers coupled into the single-mode fiber are $P_{795} = 20\ \mu$W and $P_{780} = 7\ \mu$W. The expected peak positions are marked with dashed lines.

In figure (18) the red line shows the transmission of the probe beam in the reference cell. The detuning axis is scaled such that the zero point is in the middle between the D1-transitions. The probe beam gets absorbed as long as the pump beam is off-resonant. When the pump beam is resonant, it excites some of the atoms into a different energy level and more of the 780 nm light is transmitted. For atoms with zero velocity component parallel to the beam direction this holds true at frequencies of ±181.1 MHz and the reference in figure (18) shows two strong peaks at these positions.

Because of the doppler effect different velocity classes can be addressed too. Even though the laser is locked to the $F' = 4$ transition the transitions to the $F' = 3$ and $F' = 2$ are not dipole forbidden and can be addressed if the frequency shift of the doppler effect matches the shift to these levels. The frequency shift to $f_0 = \pm 181.1$ MHz is calculated as

$$\Delta f = 4\pi^2 \frac{v_p}{\lambda_{D2}} \tag{18}$$

with v_p being the velocity parallel to the beam direction and λ_{D2} the wavelength of the locked laser. Since the shift is dependent on the wavelength the absorption peaks should be visible at

frequency shifts of

$$\Delta f_{D1} = \Delta f \frac{\lambda_{D2}}{\lambda_{D1}} \tag{19}$$

which correspond to $\Delta f_{D1} = 118.7$ MHz for the $F' = 3$ transition and $\Delta f_{D1} = 180.9$ MHz for the $F' = 2$ transition. In figure (18) these positions are marked with dashed lines and they fit the position of the peaks in the reference very well.

In comparison to the reference the signal of the fiber series is broadened. While the dominant peaks of the reference have a full width half maximum of $\mathrm{FWHM_{Ref}} = 35$ MHz the signal in the fiber series is at $\mathrm{FWHM_{Sig}} = 598$ MHz. This broadening is only slightly due to power broadening, as can be seen in figure (19) for two signals with different laser powers. For the signal with less power the full width half maximum is $\mathrm{FWHM_{Sig,weak}} = 520$ MHz.

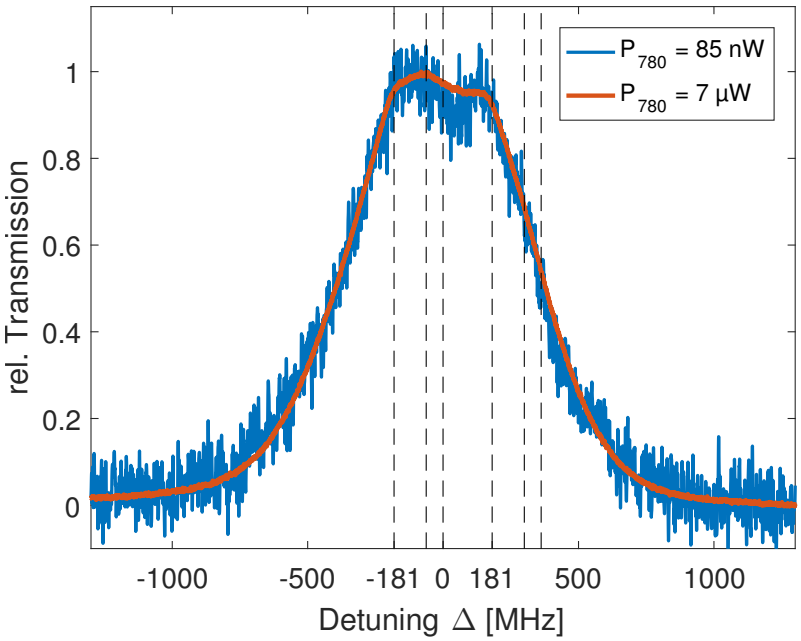

Figure 19: Sub-doppler spectroscopy with co-propagating 780 nm and 795 nm beams for different incident 780 nm laser powers. The given laser powers correspond to the power coupled into the single-mode fiber. The expected peak positions are marked with dashed lines.

The question is now, where the broadening is coming from. It could be due to transit time broadening, which occurs for atoms leaving the light field. The velocity of the atoms is Maxwell-Boltzmann distributed with a mean velocity of $\bar{v} = \sqrt{8k_BT/(\pi m)}$ and the capillary has a diameter of $d = 55\ \mu$m. The broadening is inverse to the transit-time t_T the atom stays in the light field. The shortest time would be for an atom traveling perpendicular to the beam. For a temperature of

80 °C the transit-time broadening in this system should be

$$\Delta\,\mathrm{FWHM}_{\mathrm{trans}} = \frac{1}{t_T} = \frac{\bar{v}}{d} \approx 2\pi \cdot 0.86\ \mathrm{MHz}, \tag{20}$$

which is very small and does not explain a broadening of a few 100 MHz.

Another reason could be pressure broadening through contamination with other gases. If the fiber series has a small leak air could diffuse into it. Air consists to 78% of N_2. The power broadening of the D2 line due to N_2 is given in [16] as 18.3 ± 0.2 MHz/Torr. The weak signal was broadened by 485 MHz, for this to be caused by pressure broadening with N_2 the pressure inside the fiber series has to be at 35.2 ± 0.4 mbar. This is pretty high but could be true if the fiber really has a leak somewhere.

4 Hollow Core Fibers Encapsulated in All-Glass Vapor Cell: EIT Spectroscopy

4.1 Setup

4.1.1 Cell

In the second setup the sample used is a conventional vapor cell with the modification, that it now encapsulates two hollow core fibers: one is a kagomé fiber and the other a capillary, both with similar diameters. Two of these cells are used for the experiment, one with fibers of an inner-diameter of 20 μm and the other with 60 μm. In both cases the length of the fibers is 5 cm.
In figure (20) the cells are displayed. It is filled with rubidium through the handle by the same process as the fiber series (see section 3.1.1). The handle serves as the reservoir to control the vapor density in the usual fashion. The shape of the sample is designed to fit the oven, which is described in the following section.

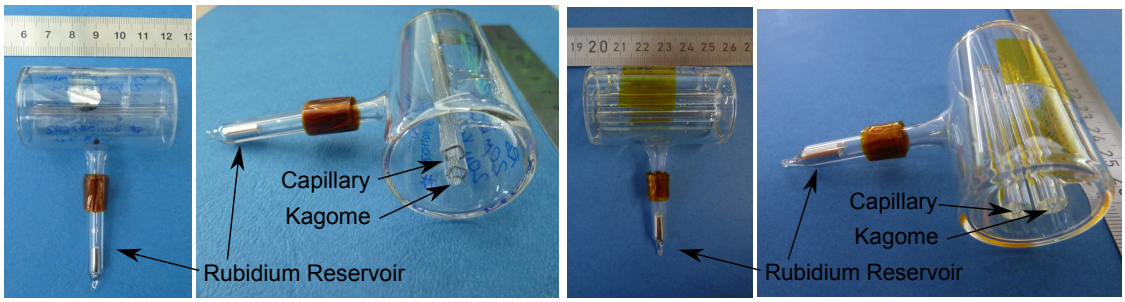

(a) 20 μm cell (b) 60 μm cell

Figure 20: Structure of the two vapor cells. Mounted inside are a kagomé and capillary with an inner diameter of (a) 20 μm and (b) 60 μm each.

4.1.2 Oven

The oven is constructed with the same concept in mind as for the fiber series. It allows the cell and the reservoir to be temperature controlled separately (see figure (21)). The handle of the cell is also wrapped polyimide tape, to help isolate between the two temperature regions. It also fixates the cell in the apparatus.

Nevertheless the isolation between the two temperature regions is not perfect. Heating the oven of the cell from room temperature up to 80 °C also results in a rise of the temperature of the reservoir to 50 °C. To achieve even higher temperature gradients active cooling elements need to be used. Tor this thesis the use of heating only was however sufficient.

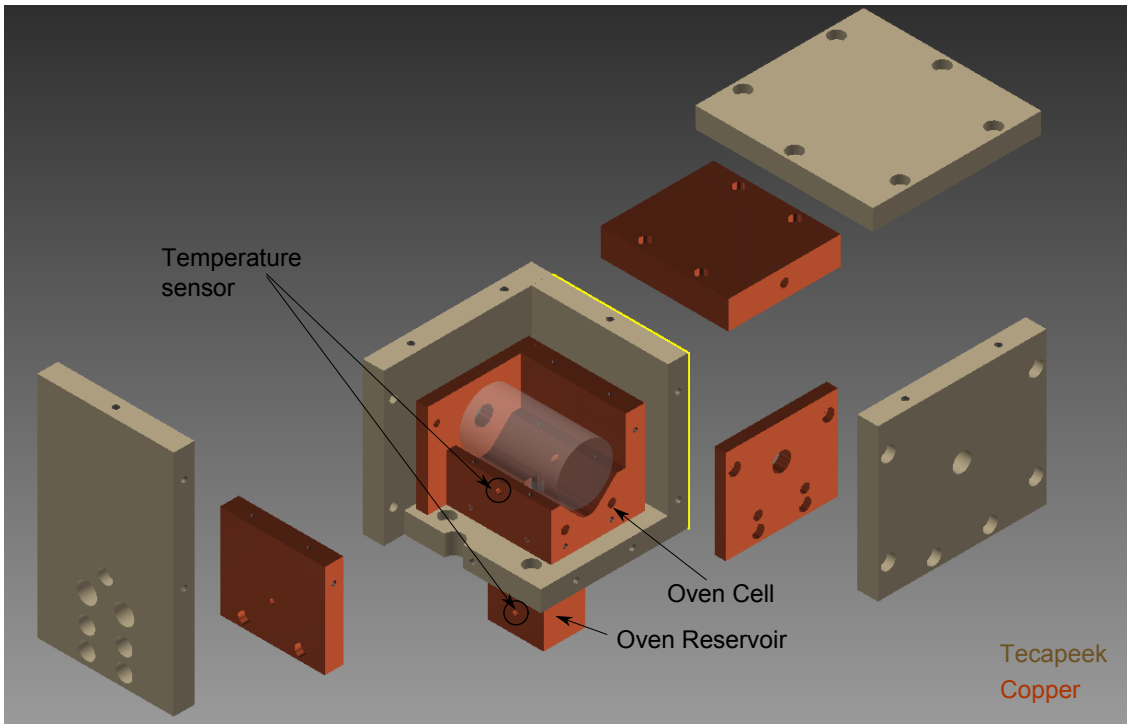

Figure 21: Schematic of the oven. The oven of the cell and the reservoir are separated with a isolating layer of tecapeek. The cell oven is also encased in tecapeek. The PT100 temperature sensors are inserted at the marked holes.

To measure the temperature PT100 probes are inserted into the holes marked in figure (21) and rest inside of the oven close to the cell respectively at the bottom of the reservoir oven. They give a good estimate about the temperature in the oven, but not about the exact temperature inside the cell. When the top cover of the oven is opened and replaced with a simple 2 mm thick glass plate, to allow "visual inspection" during spectroscopy of the fluorescence along the fiber, the PID-controller maintains the same nominal temperature inside. Measurements of the optical density however show less value, leading to the fact, that the temperature lost over the semi-open top leads to a second temperature gradient, not recognized by the temperature measurement method. Nonetheless the setup enables to heat and stabilize the temperature of the cell and the spectroscopy zone separately and gives a good estimate to control the optical density inside the cell.

4.1.3 Laser Setup

The lasers used in this setup are the red 780 nm laser (also used in the previous experiment for the D2-line absorption spectroscopy) and a blue 480 nm laser to excite the atoms to a Rydberg state. The lasers are set up in a separate room and distributed to the experiments through optical fibers.

On the optical table of the laser sources several reference spectroscopies are installed to manipulate or lock the lasers to specific transitions: For the D2-laser, a saturation-spectroscopy reference is available, to inspect the frequency scan or to lock the frequency to a specific transitions. The 480 nm light can be referenced to an EIT setup, similar to the experiment described in this chapter,but in a much larger cell.

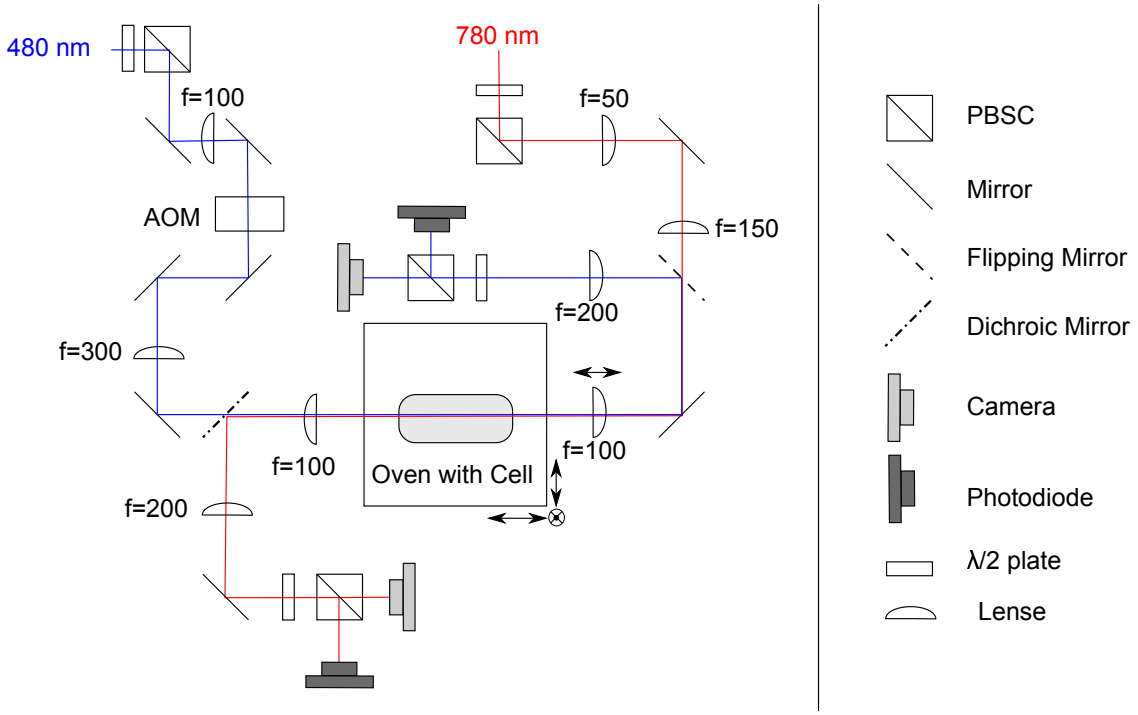

Figure 22: Schematic laser setup. The red laser is coupled into the fiber from the right side, while the blue is coupled into the fiber from the left side counter-propagating. The oven is mounted on a stage to control alignment in all three directions. The coupling is checked with the photodiodes and the ccd-cameras. The signals are detected with the photodiode on the red path.

The oven is mounted on a stage to control alignment in all three directions. This makes it easier to couple into the fibers and also switch the position to do reference measurements in the surrounding cell.

The 780 nm laser is first led through a $\lambda/2$-plate plus a polarizing beam splitter cube (PBSC) ensemble, which enables one to control the intensity of the beam. The beam is focused into the fiber with the $f = 100$ mm lens directly in front of the oven. After passing the fiber the light is collimated again with a $f = 100$ mm lens and then reflected by a dichroic mirror, which has high reflectance for the red light and good transmission for the blue light. The $f = 200$ mm lens is used

to enlarge the image of the end of the fiber and project it onto the ccd-camera. The coupling is optimized through visual confirmation of the mode form and also of the transmitted power checked with the photodiode. Later this photodiode is also used to record the absorption spectra as well as the EIT signal.

The blue 480 nm beam is set up similarly to the red beam but coupled into the fiber counter-propagating. There are only two differences: Behind the oven, instead of a dichroic mirror a flipping mirror is used since this part of the beam is only needed for the coupling process.
Additionally, the first $f = 100$ mm lens is used to focus the beam into an acoustic optical modulator (AOM). It is set up such that if the AOM is switched on, 80% of the light gets transmitted in the first mode. Through this method the strength of the blue beam coupled into the fiber can be modulated and a lock-in-amplifier can be used.

4.2 Results

4.2.1 Optical Density

The characterization of the system in comparison to the conventional system containing a vacuum-chamber and pump is of great interest. In figure (23) the filling process for the 60 μm kagomé fiber is shown. The cell had been filled with rubidium half a year ago and stored at room-temperature before the cell was heated for the first time. In figure (23a) the measurement of the optical density inside the fiber while heating the cell can be seen. At $t = 15$ min the temperature of the cell is set to $T_{\mathrm{Cell,Set}} = 80$ °C. As mentioned the reservoir and the cell are not completely temperature independent, therefore even though the set reservoir temperature is left at $T_{\mathrm{Res,Set}} = 25$ °C it rises with some delay. In response the optical density begins to rise at $t = 26$ min and saturates after approximately 20 min at a mean value of 36.9. But over the course of the next four to five days the optical density inside the fiber drops again until it stabilizes at a mean density of 5.8. This is best explained by the fact, that the sample hat been stored at room temperature for half a year and the rubidium atoms had time to diffuse into the fiber and get absorbed at the wall of the whole cell. There were also rubidium droplets inside the cell which now evaporated, leading to a fast rise of the density inside the cell and a slow equilibration of the system.

After two weaks, when the optical density was assumed to be stable, the reservoir temperature is risen to $T_{\mathrm{Res,set}} = 70$ °C as can be seen in figure (23c). The optical density reaches its maximum 6 minutes after the temperature was set. This implies a fast reaction of the system to the temperature change and a diffusion time constant in the regime of minutes. In figure (23d) this is verified when the graph of the optical density and the reservoir temperature show a very good overlap.

The optical density stays constant after the last temperature scan. However when the oven top is lifted and the tecapeek and the thick copper plate do not isolate the oven any longer the optical density drops even though the temperature measured inside the oven stays constant. This means there is a temperature gradient inside the oven and the diffusion time constant measured may not be true since the change of the optical density could be from atoms adsorbing and desorbing of the fiber wall due to temperature changes of it. Therefore LIAD measurements were done in section 4.2.2 to exclude this possible error.

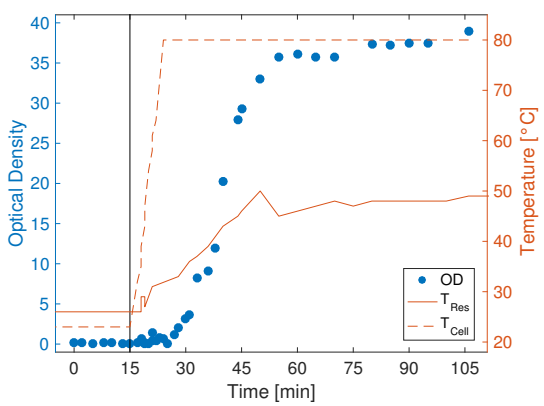

(a) Heating cell day 0

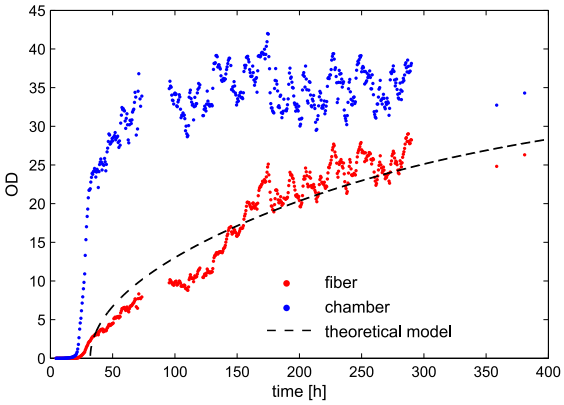

(b) Filling process of [2]

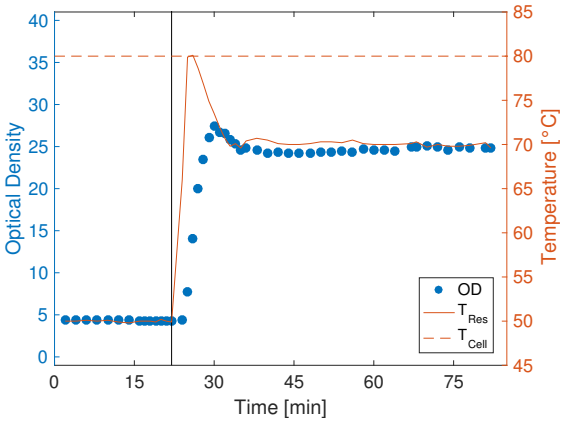

(c) Heating reservoir day 15

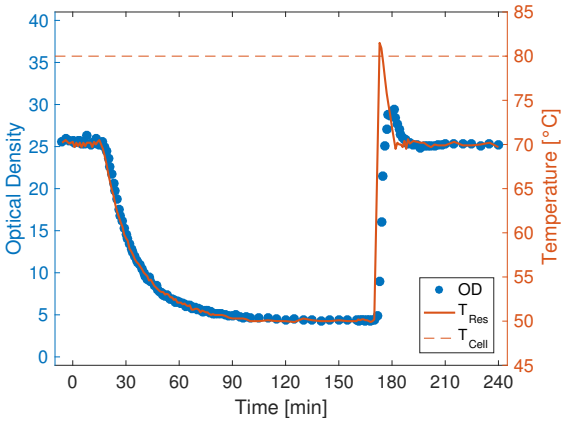

(d) Scan T_{Res} day 18

Figure 23: Optical Density inside 60 μm kagomé with temperature changes. (a) Heating of the cell to $T_{\text{Cell,set}}$ = 80 °C leaving $T_{\text{Res,set}}$ = 25 °C. (c) Setting reservoir temperature to $T_{\text{Res,set}}$ = 70°C. (d) Temperature scan $T_{\text{Res,set}}$ = 70...50...70 °C (b) Filling process of 60 μm wide and 85 mm long kagomé fiber in a conventional setup [2]. The temperatures are at T_{Res} = 45 °C and T_{Cell} = 80 °C.

In comparison to this the filling process from the master thesis of Christian Veit [2] is shown in

figure (23b) (note that the time-scale differs by a factor of 100). In this thesis the setup consists of a conventional vacuum-chamber with the fibers mounted inside and a cesium reservoir. The fiber had a length of 85 mm and an inner diameter of 60 μm . At $t = 0$ the reservoir and the cell are heated to $T_{\mathrm{Res}} = 45$ °C and $T_{\mathrm{Cell}} = 80$ °C respectively. In the first 10 hours no cesium can be detected, most likely because of the cesium atoms depositing on the wall surfaces of the vacuum chamber. But after that delay the optical density rises quickly inside the chamber and the optical density inside the fiber follows. Noticeable is here, that the time scale of the diffusion process into the fiber is in the regime of hours whereas in the case of the current thesis process happens within minutes. To explain this some facts have to be taken into account.
In [2] the fiber is first exposed to cesium at the time $t = 10$ h and from there a curing process takes place, where the atoms adsorbe on the surface and then diffuse into the glass bulk of the fiber. Therefore the atoms indeed diffuse into the fiber but do not contribute to a rise in atomic density in the fiber core. In the present thesis this curing process could not be observed due to various reasons. First of all the fiber was first exposed to the rubidium vapor during the filling process of the cell, when the cell was still connected to the vacuum pump and not in the optical set up. Secondly when the cell was ablated from the vacuum setup the optical setup was not ready yet since at that time the setup for the fiber series was installed first. So the fiber had enough time to go through the curing process.
Nevertheless the fiber cell holds some advantages in comparison to the conventional vacuum-chamber. Except for the (one time) filling process it gets by without a big vacuum setup. And the vacuum setup can be used to fill multiple cells with different fiber types with minimal cleaning effort of the vacuum parts. These cells can then easily be brought into the optical setup. Switching times between fibers are only limited to the time it takes to open and close the oven and to couple into the new fiber. If the cells are standardizes in respect to the fiber position inside the cell, the coupling time can be reduces drastically.

In figure (24) the difference in optical density of the fiber and the surrounding cell is measured for all 4 different types of fibers. For the 60 μm kagomé fiber the measurements are done with a reservoir temperature of $T_{\mathrm{Res}} = 50$ °C and for all the others for $T_{Res} = 70$ °C and an opened top, only covered with a thin 2 mm glass plate. As one can see the density inside the fibers is always a little bit lower than the density measured in the surrounding cell, namely at 90%, 93% and 75% for the 60 μm kagomé fiber, 60 μm capillary and 20 μm capillary respectively. To measure the density before and after the fiber the light is lead through the cladding. Since the fibers are only a little bit shorter than the cell the density is very low and can be neglected.

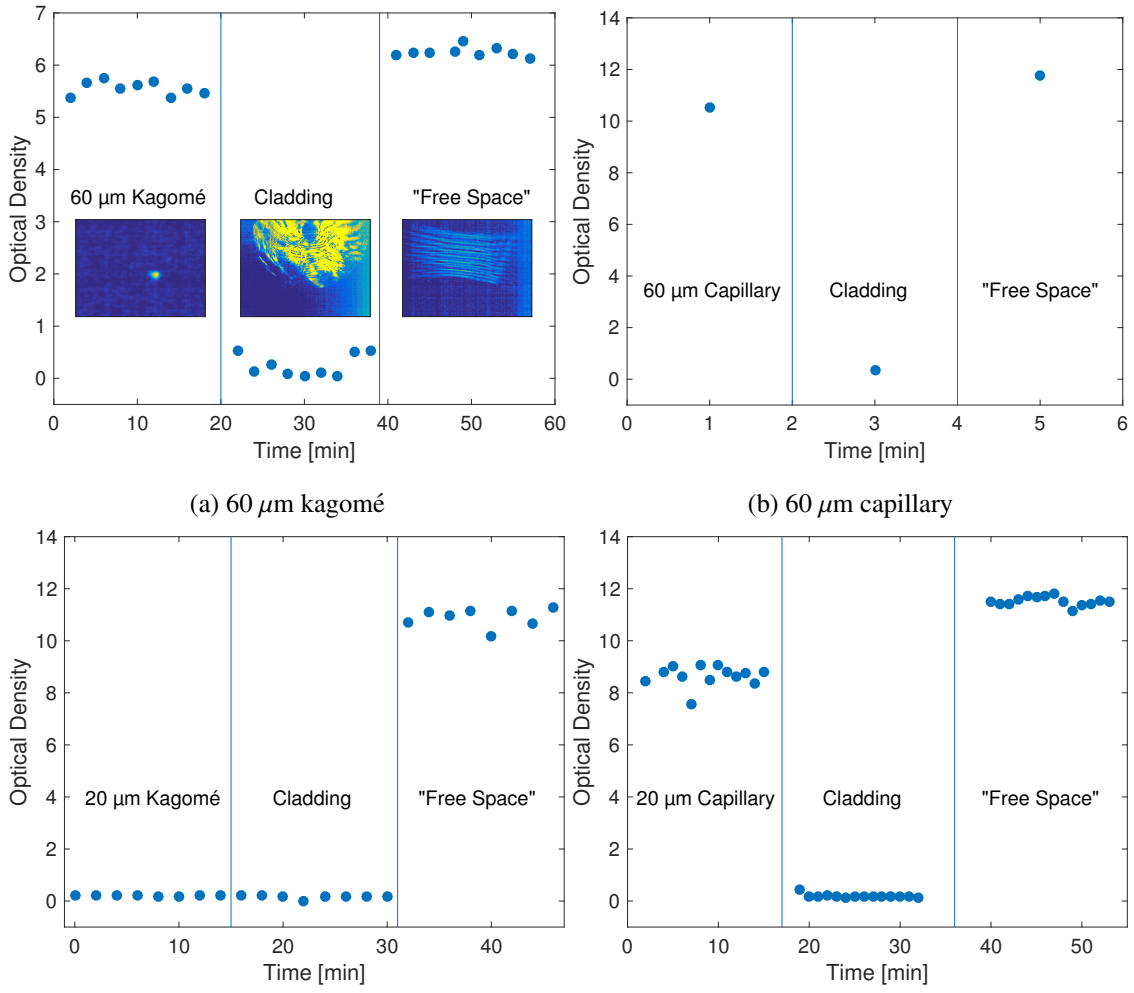

(a) 60 μm kagomé

(b) 60 μm capillary

(c) 20 μm kagomé

(d) 20 μm capillary

Figure 24: Optical density inside the different fibers and the surrounding cell. (a) $T_{Cell} = 80$ °C and $T_{Res} = 50$ °C, (b)(c)(d) $T_{Cell} = 80$ °C and $T_{Res} = 70$ °C. Insets (a) show the light guidance for the different beam paths, the "free space" is lead in between the two fibers.

For the 20 μm kagomé fiber it was very difficult to couple into and no optical density could be measured. Together with fluorescence observations of the fiber it is concluded that this fiber was damaged and therefore no further measurements were possible with it.

4.2.2 LIAD

The idea behind the LIAD experiments is to measure the diffusion in and out of the fiber without the disturbance by unknown adsorbtion and desorption processes due to temperature changes of the fiber wall. To study the effects of the LIAD, 480 nm light is used since it is already needed for the EIT measurements (see section 4.2.3) and therefore available. The blue laser light is locked to a

cavity at a frequency off-resonant to any transition to avoid distortion of the density measurements due to optical pumping or EIT effects. The optical density is monitored with the 780 nm light like before.

When the blue laser is switched on, the LIAD process is started and the optical density inside the fiber jumps up (see figure (25)). Then the atoms diffuse out of the fiber since the density outside is lower. When the blue laser is switched off, the atoms inside the fiber adsorb onto the walls again, leading to a sudden drop in density which then is evened out through diffusion into the fiber.

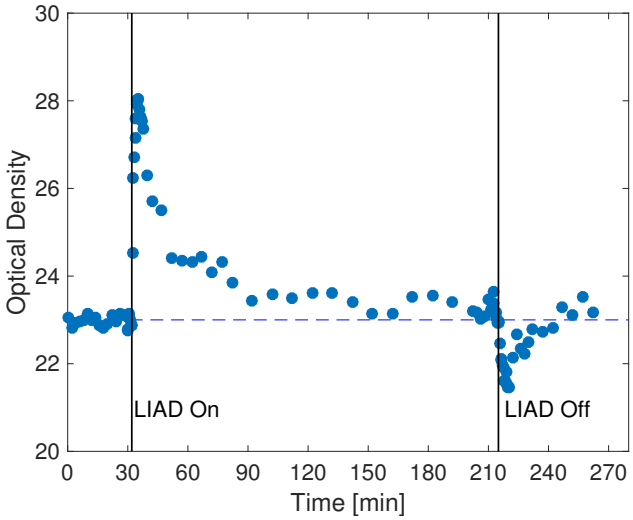

Figure 25: LIAD measurements inside 60 μm kagomé fiber with $P_{480} = 12.6$ mW. The onset (end) of the LIAD when the 480 nm laser is turned on (switched off) are marked with black lines. The dashed blue line marks the start density n_0.

To understand this in detail first a theoretical model to describe this measurement will be introduced. Afterwards the results in respect to diffusion constant and diffusion time for different LIAD laser powers and fiber diameters will be discussed.

When the light is switched on there are two processes inside the fiber. The first one is that the atoms are getting desorbed from the fiber walls and the second process is that the atoms are diffusing out of the fiber. The process can be modeled by a DGL for the density n inside the fiber:

$$\begin{aligned} \frac{\partial n(x,t)}{\partial t} &= D\frac{\partial^2 n(x,t)}{\partial x^2} - \frac{\partial n_w}{\partial t} \\ &= D\frac{\partial^2 n(x,t)}{\partial x^2} + n_w \nu_w \mathrm{e}^{-\nu_w t}, \end{aligned} \tag{21}$$

where the density of the atoms adsorbed in the fiber wall n_w is viewed as reservoir which gets opened at the time $t = 0$ and feeds the fiber with atoms at a rate ν_w. The diffusion process begins as soon as the density rises and therefore also at $t = 0$. Strictly speaking the density of the cell n_c

outside the fiber should rise because of the atoms diffusing outside, but since the volume of the cell is much larger than the fiber, n_c can be approximated to be constant throughout the measurement. The density n should equilibrate to the same value as before the LIAD. This leads to the boundary conditions for a fiber of length l of:

$$n(x, t = 0) = n_0 \qquad \text{for} \qquad -l/2 \leq x \leq l/2 \tag{22}$$

$$n(x = \pm l/2, t) = n_0. \tag{23}$$

With this the numerical solution for eq. (21) can be computed. In the case of switching off the blue light, only the sign in front of the desorption term changes in eq. (21). Now the wall is seen as a drain and n_w is the density of atoms getting absorbed into the fiber wall with the rate ν_w. Since the optical density is proportional to the atomic density, this simulation can be transferred directly to the measurements.

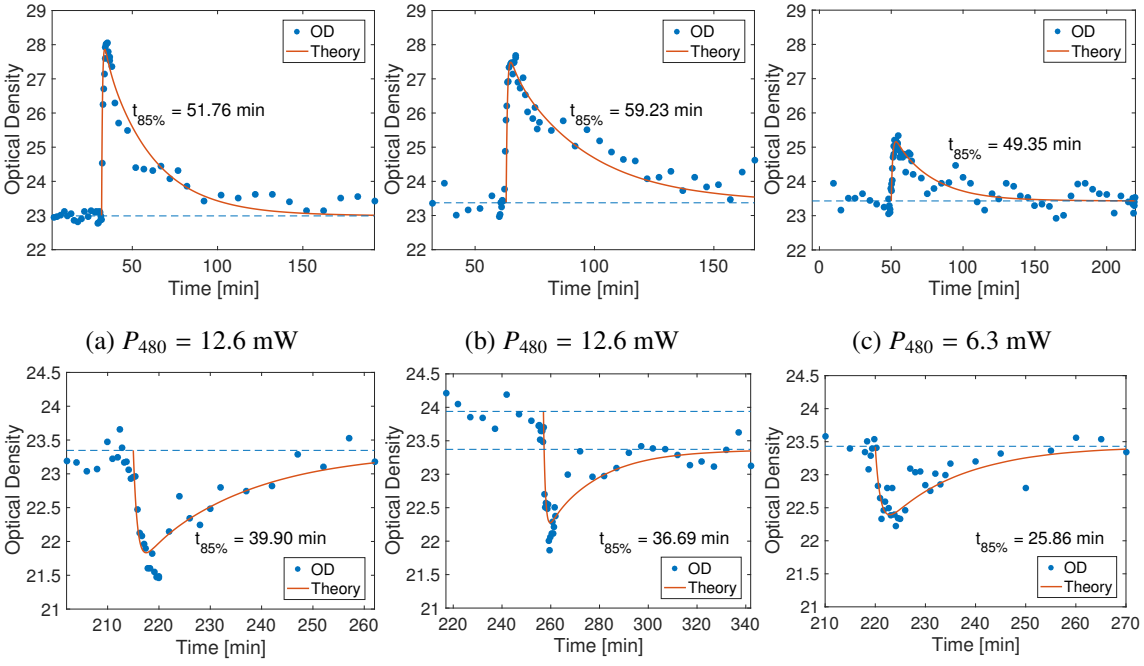

(a) P_{480} = 12.6 mW (b) P_{480} = 12.6 mW (c) P_{480} = 6.3 mW

(d) P_{480} = 12.6 mW (e) P_{480} = 12.6 mW (f) P_{480} = 6.3 mW

Figure 26: LIAD measurements in 60 μm kagomé fiber for different blue laser powers. The blue dashed line marks the start density n_0 and the end density used for the simulations. Except for case (e) start and end density are the same. In (e) the system was not equilibrated again before the laser was turned off leading to a higher start density.

In figure (26) three such measurements with different LIAD laser powers can be seen for the 60 μm kagomé fiber. The top line shows the OD when the blue light is switched on, while the

bottom line shows the behavior for the same measurement when the light is switched off again. Additionally the numerical simulations are shown, whereas D, n_w and τ_w are chosen to fit the experiment data. In [2] and [3] the "filling time" is defined as the duration until the density inside the fiber reaches 85% of the surrounding density in equation (14). Following this line of thought here a time $t_{85\%}$ is defined as the time when the difference of n to n_0 reaches $1 - 0.85 \mathrel{\hat{=}} 15\%$ of $\max(n - n_0)$. These times are also depicted in figure (26).

As one can see $t_{85\%}$ lies in the range of half an hour to an hour for the 60 μm kagomé fiber. The diffusion process into the fiber surprisingly seems to be faster than out of it. It is however independent from the LIAD laser power and only n_w changes as can be seen in table (4). For half the laser power the atoms desorbing approximately also halves. The number of atoms absorbing into the surface when the laser is switched off on the other hand seems to be independent from the incident laser power. This is plausible since this should only be dependent on the number of atoms available to adsorb into the fiber wall.

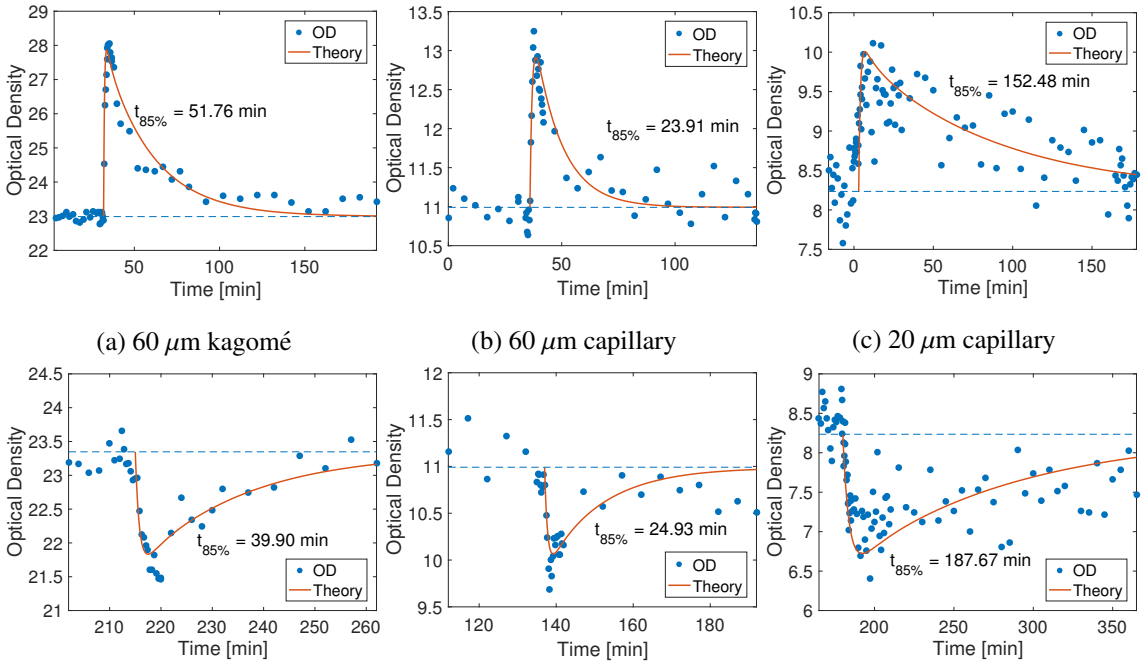

(a) 60 μm kagomé (b) 60 μm capillary (c) 20 μm capillary

(d) 60 μm kagomé (e) 60 μm capillary (f) 20 μm capillary

Figure 27: LIAD measurements in different fibers. The laser power for (a) is at $P_{480} = 12.6$ mW and for (b),(c) at 10.0 mW. The blue dashed lines mark the start density n_0 and the end density used for the simulations. Start and end density match for all measurements.

To take a closer look at the diffusion process the diffusion constant and adsorption time give a good means of comparison. The diffusion constant D is, as expected, independent of the LIAD

laser power. For the measurements in the 60 μm kagomé it is in the order of 10^{-7} $\frac{m^2}{s}$. The absorption time τ is in the order of ms. If the theoretical values for these parameters are calculated after eq. (12) for $E_a = 0.66$ eV [12] and $\tau_0 = 1 \cdot 10^{-13}$ [17] at a temperature of 80 °C it yields $\tau_{\text{theo}} = 0.26$ ms and $D_{\text{theo}} = 4.5 \cdot 10^{-6}$ $\frac{m^2}{s}$. The measured values are only an order of magnitude apart from this.

Fiber	$t_{85\%}$ [min]	D [m^2/s]	τ [ms]	$t_{85\%}$ [min]	D [m^2/s]	τ [ms]
60 μm kagomé	51.76	$0.15 \cdot 10^{-6}$	8	39.90	$0.20 \cdot 10^{-6}$	6
	59.23	$0.13 \cdot 10^{-6}$	9	36.69	$0.20 \cdot 10^{-6}$	6
	49.35	$0.16 \cdot 10^{-6}$	8	25.86	$0.28 \cdot 10^{-6}$	4
60 μm capillary	23.91	$0.34 \cdot 10^{-6}$	3	24.93	$0.30 \cdot 10^{-6}$	3
20 μm capillary	152.48	$0.05 \cdot 10^{-6}$	3	187.67	$0.04 \cdot 10^{-6}$	3
theor. for 60 μm	-	-	-	-	$4.5 \cdot 10^{-6}$	0.26

Table 3: Comparison for the diffusion out of (left) and into (right) the fibers. The theoretical value was calculated for values E_a and τ_0 taken from [12, 17] respectively.

In figure (27) the LIAD measurements can be seen for the different fibers. After eq. (14) the filling process should only be dependent on the fiber radius r, the length l and the temperature of the wall T_w and the molecules T. Since in this case the T_w and T can not be measured separately, $T_w = T$ is assumed. As $T_{\text{Cell,set}} = 80$ °C holds true for all measurements and all fibers have the same length, the diffusion time $t_{85\%}$ should only differ for different fiber radii r. The measurements for the capillaries are done without the copper top cover of the oven and therefore the density inside the fiber and surrounding is lower than at the kagomé measurements. Comparing the measurements of the 60 μm capillary and the 20 μm capillary the value of the diffusion constant decreased an order. This is expected since

$$D = \frac{4}{3} \frac{r^2}{\tau + (2r/\bar{v})}. \tag{24}$$

and since $\frac{2r}{\bar{v}}$ in this system is six orders smaller than τ, $D \propto r^2$ is approximately true. So reducing the radius of the capillary by a factor of 3 should yield a diffusion constant decreased by a factor of 9.

For better comparison purposes the simulated fits for the different cases are shown together in figure (28). Here ΔOD is the difference of the optical density to the density at the beginning of the measurement. The red and the violet curve only differ in LIAD laser power and the blue and green line only in fiber diameter. It is clearly visible that for different laser powers the maximal optical

density for the desorption process varies accordingly. For the adsorption process the minimal optical density stays more constant. For different fiber diameters the diffusion time $t_{85\%}$ is the changing parameter.

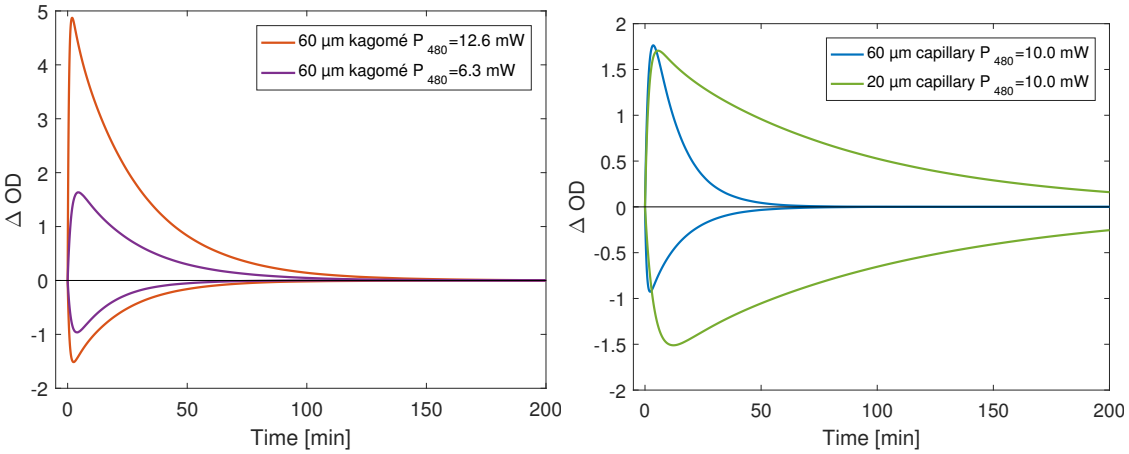

(a) Different laser powers

(b) Different fiber diameters

Figure 28: LIAD comparison for different laser powers (a) and fiber inner diameters (b). The depicted graphs are the fitted simulations from the measurements shown in figure (26) and figure (27) and show both the desorption and the adsorption process.

Lastly a look at the LIAD process enabling these diffusion measurements is taken. The values from the desorption, respectively adsorption process in the fibers are listed in table (4).

Fiber	Power [mW]	n_w	τ_w [s]	n_w	τ_w [s]
60 μm kagomé	12.6	6	33	2	50
	12.6	5	33	2	50
	6.3	2.3	100	1.5	100
60 μm capillary	10.0	2.9	100	1.3	50
20 μm capillary	10.0	2.1	100	2	250

Table 4: Comparison for the desorption process when the LIAD light is turned on (left) and the adsorption process when the LIAD light is turned off (right) for different laser powers and fibers. The time constant $\tau_w = 1/\nu_w$ is the inverse desorption (adsorption) rate of the model in eq.(21).

Strikingly the values of τ_w are a lot lager than those for τ in table (3). This means the desorption (adsorption) process is a lot slower than anticipated. In [18] the LIAD process for rubidium in fibers with a 806 nm laser was examined. Here the optical density rose instantaneously in the

timescale of ms as soon as the LIAD light was switched on. In the experiments performed in this thesis, the optical density however needs 2 to 5 minutes till it reaches its maximum. This leads to the conclusion that the desorption effects observed here are slow effects like the SPID and not LIAD in the strict sense.

4.2.3 EIT

For the EIT measurements there are two interesting regimes. The high laser power regime to observe optical bistabilities and the low laser power regime to achieve narrow line width of the EIT signal and thereby optical non-linearities.

To do this measurements the 780 nm laser is locked to the transition from ^{85}Rb $5^2S_{1/2}$ $F = 3$ to $5^2P_{3/2}$ $F' = 4$ (see figure (29a)). The 480 nm laser is frequency scanned over the transition from $5^2P_{3/2}$ $F' = 4$ to $22^2S_{1/2}$ $F'' = 3$ and the relative frequency is determined with a Fabry-Pérot interferometer. The transmission is recorded in both scanning directions. In figure (29b) the scan is first performed from red-detuned to blue-detuned and then in the other direction. The arrows are always pointing from the red-detuned to blue-detuned. During the measurement the 480 nm

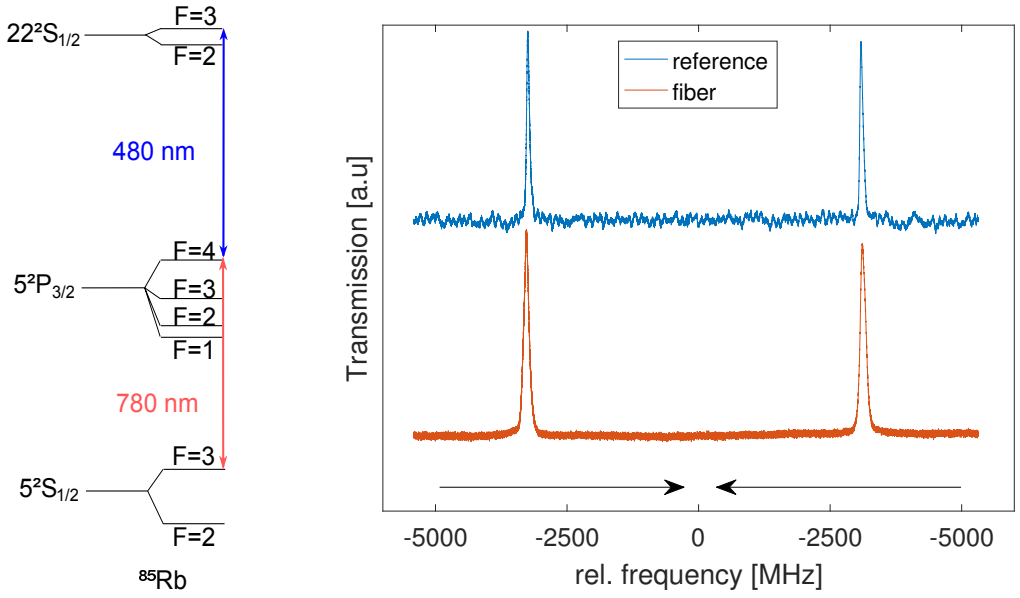

(a) EIT excitation scheme

(b) Measurement

Figure 29: Measurement method for the EIT. (a) The 780 nm laser serves as weak probe beam and is locked to its transition, whereas the 480 nm laser serves as strong coupling beam and is frequency scanned around its transition. (b) Exemplary spectra of the fiber and the reference in a conventional vapor cell. The spectra is first scanned from the red-detuned side to the blue-detuned and then the other way around.

laser is intensity modulated with the AOM at a frequency of 20 kHz and the signal is then recorded with a lock-in amplifier. The amplifier has a delay time which leads to a frequency offset in the spectra. This offset has an opposite sign for the two scanning directions and can be compensated. The given shifts in the following evaluation are therefore the mean value of the shifts for the two scanning directions. The zero point of the frequency axis in the following graphs is given by the position of the reference measurements, with the offset subtracted out.

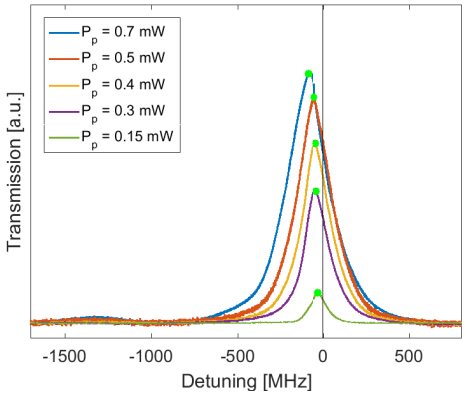

(a) 60 μm kagomé with P_c = 10 mW

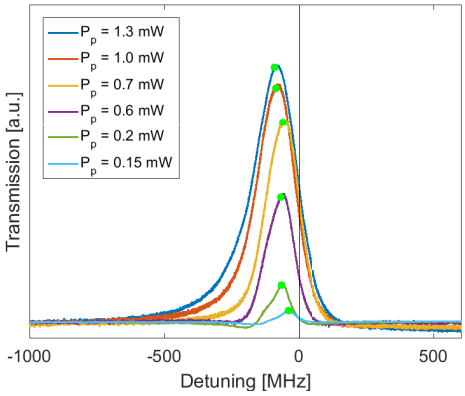

(b) 60 μm capillary with P_c = 10 mW

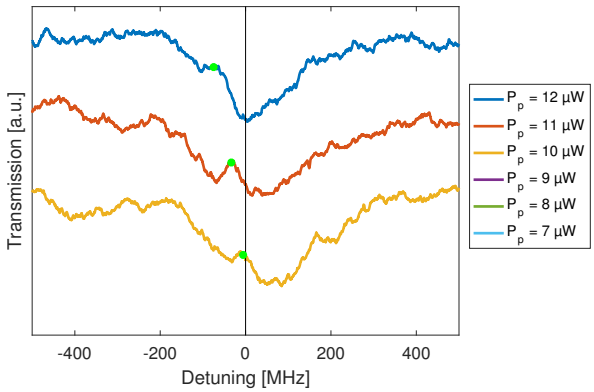

(c) 20 μm capillary P_c = 1.1 mW

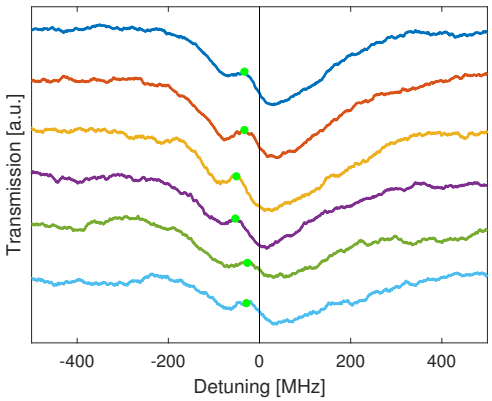

(d) 20 μm capillary P_c = 2.2 mW

Figure 30: EIT spectra for different fiber types, coupling laser powers P_c and probe laser powers P_p. The given values of the laser power are prior to coupling into the fiber.

In figure (30) the EIT signals measured in the different fiber types are shown. The spectra for the fibers with 60 μm are averaged $\approx$ 20 times. The ones for the 20 μm capillary are averaged $>$ 800 times and subsequently the data is smoothed using a moving average. For the 60 μm fibers the coupling efficiency for the probe beam is at 29% and the coupling beam at 10%. For the 20 μm capillary it is at 10% for the probe and 5% for the coupling respectively. The given laser powers in the figures are the laser powers in front of the fiber prior to coupling into it.

First a look at the high laser power regime is taken and the observed shifts are discussed. As one can see the red-shift of the signal gets larger with rising probe power. To measure this, the spectra for the 60 μm fibers are fitted with a Lorentz and the shift is read out. The peak positions are marked with green dots in the signal figures and the shift over the probe power is depicted in figure (31). The vertical errorbars originate form uncertainties from the offset from the lock-in and the horizontal from fluctuations of the laser power.

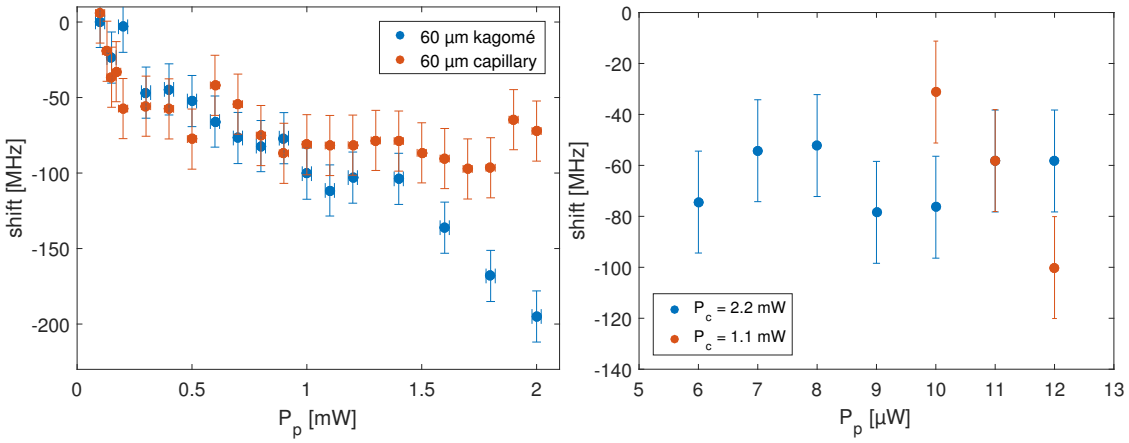

(a) Shift in the 60 μm fibers for P_c = 10 mW.

(b) Shift in the 20 μm capillary for different P_c.

Figure 31: Measured shifts for the different fibers. The given laser powers are prior to coupling.

In contrast to measurements in [2] and [12], where the shift diminishes with rising probe power, here it grows larger. In [12] the reasoning is that with rising probe beam power the Rydberg state population grows larger and this leads to an increased flux of collision ionized electrons. These electrons can then bind to the surface of the fiber walls and weaken the e-field. A weaker e-field should mean a weaker ac stark shift. But [2] has weak probe powers near the saturation intensity, whereas in the case presented here, the laser powers are far above saturation, which should be at $P_{p,\mathrm{Sat}}$ = 70 nW for a beamwaist of 60 μm. Therefore the shift has to have a different source.

For high laser powers optical bistability was observed in a conventional vapor cell by [14]. Here increasing shifts for increasing laser powers were recorded. The source for the bistability as for the shifts was explained by ions. The high Rydberg state population leads to an increase in collision ionized electrons and at the same time ions remain back. The electrons are fast moving and leave the interaction region quickly, and in the case of the fiber this is even enhanced through electrons binding to the surface. The remaining (slower since heavier) ions take a while to diffuse out of the interaction region. In the case of the fiber they take even longer, but on the same time, if they hit the wall they can get adsorbed or they can recombine with a bound electron. Nevertheless the

number of ions should increase with increasing power of the probe beam and the shift should get larger.

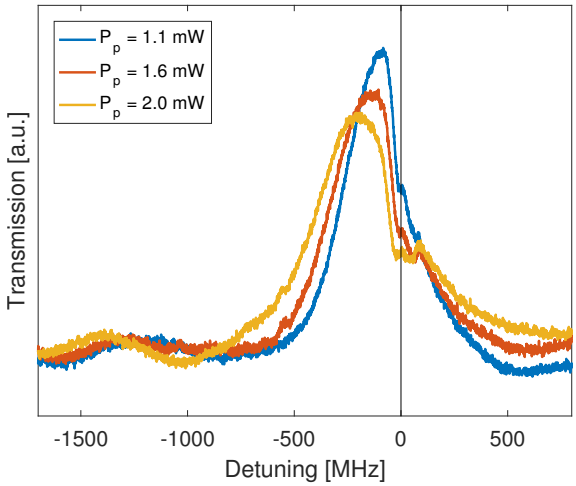

Figure 32: EIT signals for high probe powers recorded without modulating the coupling beam with the AOM. The signal resembles the bistability signal from [19] but shows no hysteresis.

In conclusion the observed shift in these measurements is not due to atom-wall interactions but rather atom-ion interaction. It would be interesting if bistability is possible to observe in hollow core fibers. To achieve this the AOM is switched off, since bistability can not be observed with a modulated coupling beam, and the power off the probe beam was risen ever higher. The resulting signal seen in figure (32) resembles the bistability signal in [19], but shows no hysteresis but rather a perfect overlap for the frequency scan in different directions. It seems that bistability can not be obtained because the lifetime of the excitation is limited through the atom collisions with the wall.

The EIT for high laser powers is also recorded in the 20 μm capillary. As can be seen in (30c) and (30d) the signal is clearly different from the signal observed in the broader 60 μm fibers. Since it is very weak it has to be averaged over a long time span. If the lock of the laser drifted during the time the signal drifted as well, leading to the high error-bars of figure (31b). For a coupling laser power of $P_c = 2.2$ mW the shift seems to stay constant whereas for lower coupling powers $P_c = 1.1$ mW the shift seems to increase for rising probe laser power P_p (see also figure(30c)), similar to the 60 μm fibers. But the errors are to large to make a definitive statement.

On the other hand the weak power regime is also interesting for obtaining narrow line widths of the EIT peak. In [4] EIT signals in a rubidium filled hollow core fiber were examined. For weak coupling powers of up to a maximum of 2 μW and a probe power of 1.6 μW they achieved a minimal width of 6 MHz in a Λ-type level configuration.

In this thesis the EIT signal in the 60 μm fibers vanished for incoupled probe powers below

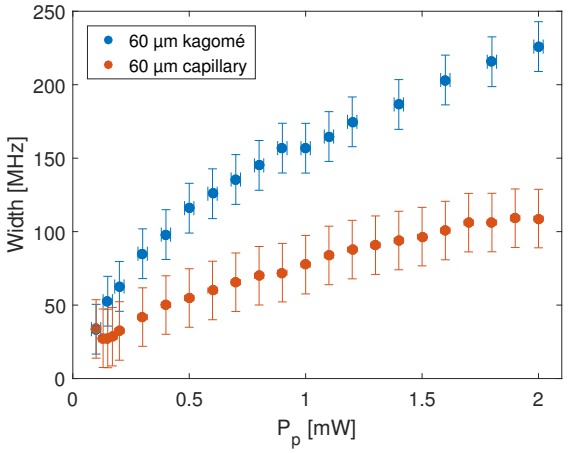

Figure 33: EIT width for the 60 μm fibers. For probe powers smaller 0.1 mW the signal vanished. The smallest width observed are at 33 MHz and 27 MHz for the kagomé and capillary respectively.

P_p = 100 μW indifferent of the coupling laser power. For the achieved coupling efficiency of 29 % this would mean a probe laser power inside the fiber of $P_{p,\text{inside}}$ = 28 μW. At this point the width for the 60 μm kagomé and capillary is at 33 MHz and 27 MHz respectively (see figure (33)). For the present excitation scheme this seems to be the limit.

5 Conclusion and Outlook

The aim of this thesis was to gain further insight into the combination of Rydberg spectroscopy in atomic vapor with hollow core optical fibers. Therefore, two different sample types of hollow core fibers were examined. One was the fiber series and the other a conventional vapor cell with two hollow core fibers mounted inside.

The fiber series is a step towards miniaturized optical devices for electromagnetic field measurements. The setup of a single-mode optical fiber placed in series with a glass capillary followed by a multi-mode optical fiber had a transmission efficiency of 4.4% respectively 6.6% for the single-mode to multi-mode transmission direction, which is in the expected regime of $\approx 5\%$. In the reverse direction, the transmission was lower, namely at 0.01% and 0.03% respectively, but still non-zero. Absorption spectroscopy measurements could be done in both directions, but sub-doppler spectroscopy proved to be challenging due to an interference signal of unknown origin for light traveling in the multi-mode to single-mode direction. Measurements with co-propagating beams in the single-mode to multi-mode direction lead to strongly broadened "Lamb dips". The broadening is most likely due to pressure broadening effects.

Nevertheless the principle of the device is proven to be working. Additional measurements should be done with different samples to clarify the origin of the interference signal and the broadening mechanism for the sub-doppler regime.

The second sample type consists of a capillary and a hollow core kagomé photonic crystal fiber, both mounted in a conventional all glass vapor cell. They each had the same inner-diameter. Two of these samples were prepared, one with fibers of a inner-diameter of 60 μm and the other with 20 μm. LIAD measurements inside this fibers showed that the diffusion process is strongly dependent on the core diameter, with smaller core sizes leading to longer diffusion times. For the 60 μm fibers the diffusion constants were in the order of $10^{-7}\,\frac{\mathrm{m}^2}{\mathrm{s}}$. Predictions from theoretical calculations lead to diffusion constants in the order of $10^{-6}\,\frac{\mathrm{m}^2}{\mathrm{s}}$, which is only one order of magnitude apart. The measured diffusion constant for the 20 μm fibers was at the order of $10^{-8}\,\frac{\mathrm{m}^2}{\mathrm{s}}$. Like it was expected it is an order smaller than the diffusion in the 3 times wider fibers.

Finally EIT measurements with counter-propagating probe and coupling beams were performed. For high laser powers the signal showed a red-shift which is contributed to collision ionization of the Rydberg states. These ions interact with the Rydberg atoms and produce a energy shift which rises with increasing ion population. The search for a bistability signal resulting from those Rydberg-ion interactions lead to no finding. This is most likely contributed to the fact that the

bistable states can not be sustained long enough due to collisions with the fiber wall. For weaker laser powers the width of the signal was observed in order to evaluate the feasibility of non-linear optics. There was a lower limit of the probe beam power under which the EIT signal vanished. At this point the width was in the range of 30 MHz. Further measurements should be conducted so examine what steps have to be taken to reduce this line width further. For example reducing the atomic density inside the fibers could lead to EIT signals with lower laser powers.

Nevertheless the results for the two different fiber samples showed that bulky vacuum-chambers are no longer necessary and an important step in the direction of generating miniaturized, integrable, room-temperature devices was achieved.

Bibliography

[1] Rolf Heidemann, Ulrich Raitzsch, Vera Bendkowsky, Bjorn Butscher, Robert Low, Luis Santos, and Tilman Pfau. Evidence for coherent collective rydberg excitation in the strong blockade regime. *Physical review letters*, 99(16):163601, 2007.

[2] Christian Veit. Rf dressing of rydberg states in hollow-core fibers: Master thesis. *Universität Stuttgart*, 2015.

[3] Kathrin Kleinbach. Rydberg spectroscopy in hollow core fibers: Master thesis. *Universität Stuttgart*, 2014.

[4] P. S. Light, F. Benabid, F. Couny, M. Maric, and A. N. Luiten. Electromagnetically induced transparency in rb-filled coated hollow-core photonic crystal fiber. *Opt. Lett.*, 32(10):1323–1325, 2007.

[5] Daniel A. Steck. *Alkali D Line Data*. Version 2.1.4. http://steck.us/alkalidata, 2010.

[6] Wolfgang Demtröder. *Laserspektroskopie 1: Grundlagen*. SpringerLink : Bücher. Springer-Verlag Berlin Heidelberg, Berlin and Heidelberg, 6., aktualisierte auflage edition, 2011.

[7] Wolfgang Demtröder. *Laserspektroskopie 2: Experimentelle Techniken*. Springer, Berlin, 6. neu bearbeitete und aktualisierte auflage edition, 2013.

[8] Rick K. Nubling. Launch conditions and mode coupling in hollow-glass waveguides. *Optical Engineering*, 37(9):2454, 1998.

[9] G. J. Pearce, G. S. Wiederhecker, C. G. Poulton, S. Burger, and P. St. J. Russell. Models for guidance in kagome-structured hollow-core photonic crystal fibres. *Optics Express*, 15(20):12680, 2007.

[10] P. Clausing. Über die adsorptionszeit und ihre messung durch strömungsversuche. *Annalen der Physik*, 399(4):489–520, 1930.

[11] A. Burchianti, A. Bogi, C. Marinelli, C. Maibohm, E. Mariotti, S. Sanguinetti, and L. Moi. Optical characterization and manipulation of alkali metal nanoparticles in porous silica. *The European Physical Journal D*, 49(2):201–210, 2008.

[12] J. A. Sedlacek, E. Kim, S. T. Rittenhouse, P. F. Weck, H. R. Sadeghpour, and J. P. Shaffer. Electric field cancellation on quartz by rb adsorbate-induced negative electron affinity. *Physical review letters*, 116(13):133201, 2016.

[13] Michael Fleischhauer, Atac Imamoglu, and Jonathan P. Marangos. Electromagnetically induced transparency: Optics in coherent media. *Rev. Mod. Phys.*, 77(2):633–673, 2005.

[14] Daniel Weller, Alban Urvoy, Andy Rico, Robert Löw, and Harald Kübler. Charge-induced optical bistability in thermal rydberg vapor. *Physical Review A*, 94(6), 2016.

[15] C. Carr, R. Ritter, C. G. Wade, C. S. Adams, and K. J. Weatherill. Nonequilibrium phase transition in a dilute rydberg ensemble. *Physical review letters*, 111(11):113901, 2013.

[16] Matthew Don Rotondaro. Collisional dynamics of the rubidium 5^2p levels: Dissertation. 1995.

[17] de Boer, J. H. *The dynamical character of adsorption*. Clarendon Press, Oxford, 1968.

[18] Amar R. Bhagwat, Aaron D. Slepkov, Vivek Venkataraman, Pablo Londero, and Alexander L. Gaeta. On-demand all-optical generation of controlled rb-vapor densities in photonic-band-gap fibers. *Physical Review A*, 79(6), 2009.

[19] D. S. Ding, C. S. Adams, B. S. Shi, G. C. Guo. Non-equilibrium phase-transitions in multi-component rydberg gases. 2016.

Danksagung

Zuerst danke ich meinen Eltern, ohne die mir diese Studium nicht möglich gewesen wäre und die mich die ganzen letzten Jahre wunderbar und unübertrefflich unterstützt haben.

Dann danke ich allen Mitarbeitern des Instituts und ganz besonders allen aus dem 3.Stock. Für all die vielen nützlichen Ratschläge, Anregungen und Hilfestellungen die ihr mir das letzte Jahr über habt zukommen lassen. Ganz besonders danke ich Daniel Weller, der immer mit einer helfenden Hand da war und mich sehr gut betreut hat. Vielen Dank auch für das unermüdliche Korrekturlesen dieser Arbeit.

Nicht zuletzt bedanke ich mich bei meinen Freunden und Komilitonen, die immer da waren um auch mal ein Problem auszudiskutieren, wenn ich einen Knoten im Kopf lösen musste.